Flow Accelerated Corrosion in Nuclear Power Plants: A Detailed Review on Mechanisms, Mitigation, and Management

3

1

2

- Malik Al-Abed Allah ^a, Mohammed Arroussi ^b, Osman K. Siddiqui ^{a, b}, Muhammad Yusuf ^b,
 Timothy N. Hunter ^c, Afaque Shams ^{a, b}, Ihsan ul Haq Toor ^{a, d, 1,}
- 6 ^a Department of Mechanical Engineering, King Fahd University of Petroleum and Minerals
- 7 (KFUPM), Dhahran 31261, Kingdom of Saudi Arabia
- 8 b Interdisciplinary Research Center for Industrial Nuclear Energy (IRC-INE), King Fahd
- 9 University of Petroleum and Minerals (KFUPM), Dhahran 31261, Saudi Arabia
- 10 ° School of Chemical and Process Engineering, University of Leeds, Leeds LS2 9JT, United
- 11 Kingdom
- 12 d Interdisciplinary Research Center for Advanced Materials (IRC-AM), King Fahd University
- of Petroleum and Minerals (KFUPM), Dhahran 31261, Saudi Arabia

Abstract

14

15

16

17

18

19

20

21

22

23

24

25

26

27

28

29

30

31

Flow-Accelerated Corrosion (FAC) is one of the most critical degradation mechanisms in nuclear power plants (NPPs), particularly affecting carbon steel components exposed to hightemperature water and steam flows. This review provides a comprehensive overview of FAC mechanisms, highlighting the electrochemical and mass transfer processes responsible for oxide film dissolution and metal loss. Predictive modeling approaches, ranging from semiempirical models to modern computational fluid dynamics (CFD) and machine learning (ML) techniques, are discussed in terms of their capability to forecast FAC progression under varied operational scenarios. Factors influencing the FAC rate of metals, including the environmental parameters and material composition, are discussed in detail. A detailed overview of experimental testing methods—including stirred autoclaves, jet impingement setups, and rotating cage systems—is provided, along with their limitations in replicating real-world reactor conditions. The paper also outlines the current mitigation strategies, including metal formulation, chemical inhibitors, and maintenance strategies for suitable operation in NPP. Recent advances highlight the role of alloying elements such as chromium (Cr) and molybdenum (Mo) in stabilizing protective oxide layers, while also revealing important limitations of CFD models (e.g., challenges in validation and surface kinetics integration) and ML methods (e.g., lack of interpretability and regulatory readiness). Future research directions

man address. Insume krapin.edu.sa, toorinsume ginam.eom

¹ Corresponding author. Tel. :+966-13-860-7493; Fax. :+ 966-13-860 2949; E-mail address: ihsan@kfupm.edu.sa, toorihsan@gmail.com

- 32 emphasize the need for integrated, multi-physics models, real-time monitoring systems, and
- 33 the development of advanced materials to ensure long-term structural integrity and safety in
- 34 next-generation nuclear reactors.
- 35 Keywords: Flow-accelerated corrosion; Carbon steel; Low alloy steel; Nuclear power plants.

1. Introduction

- Nuclear power plants (NPPs) play a key role in delivering reliable, environmentally
- 38 beneficial energy at competitive costs. As a consequence of increased global energy
- 39 consumption and focus on reducing dependency on fossil fuels, nuclear energy is emerging as
- a very important technology that can meet energy requirements on a large scale [1], [2], with
- 41 low carbon emissions [3], [4]. However, metals used in NPPs suffer from corrosion, which
- 42 leads to a serious degradation of equipment and pipes, potential leaks, environmental
- 43 contamination, and safety risks [5], [6], [7].
- 44 Flow-accelerated corrosion (FAC) is a primary degradation mode in NPP, compromising
- 45 the structural stability of piping systems, heat exchangers, and essential components [5].
- 46 Among the various types of corrosion in NPPs, FAC is particularly significant because of its
- 47 frequency and operational impact, together with stress corrosion cracking (SCC) [8],
- 48 microbiologically influenced corrosion (MIC) [9], primary water stress corrosion cracking
- 49 (PWSCC) [10], sensitized intergranular stress corrosion cracking (IGSCC) [11], irradiation-
- assisted corrosion [12], and hydrogen-induced corrosion [13]. In NPPs, FAC occurs when
- 51 metals undergo high temperature and pressure, particularly within feedwater and condensate
- 52 systems [14]. FAC originates from the complex interaction between flowing of water, metal
- surfaces, and operational parameters in NPPs [15], [16]. About 17% of reported FAC events
- resulted in operational restrictions or forced outages. This highlights the critical importance of
- addressing FAC within the NPP infrastructure.
- There are many factors that can affect the FAC rate of metals. These are broadly classified
- 57 into three categories, including (1) hydrodynamic factors, e.g., mass transfer, (2) water
- 58 chemical factors, e.g., dissolved oxygen, pH, temperature, and (3) material factors e.g., alloying
- elements, content of alloying elements, passive film [17], [18]. For instance, the changes in
- 60 turbulent flow conditions, shear stress areas, pipe restrictions, and abrupt shape have been
- 61 found to accelerate the removal of protective oxides [19]. The addition of 2 μg/kg oxygen in
- 62 neutral and alkaline solutions significantly reduced the FAC rate of carbon steel, suggesting
- 63 that dissolved oxygen is a critical factor in FAC [20], [21]. In the case of temperature, the FAC
- rate depends on the type of metal, but carbon steel exhibits the maximum FAC rate at 130-150

65 °C in neutral and alkaline solutions [22]. The FAC rates are affected by the solubility of the surface oxide, which exhibits an inversion in temperature dependence within the pH range of 66 9.8–10.3, forming distinctive surface patterns [5]. From the perspective of material factors, the 67 addition of alloying elements such as Cr, Ce, and Cu into pipeline steel has been found to affect 68 FAC [23], [24]. Cr significantly enriches the Fe₃O4 layer, which enhances the corrosion 69 resistance of the welded steel against FAC [24]. Thus, understanding the mechanism through 70 71 which these factors initiate and /or accelerate the FAC rate is essential to develop anti-FAC 72 strategies and guarantee the long-term safety and sustainable operation of power plants [25]. 73 Inhibition of FAC is a key concern for the suitable operation of NPPs. Many methods have 74 been used to mitigate the FAC including metal formulation [26], [14], e.g., 2.25Cr-1Mo, 75 SA335-SA106, chemical inhibitors, e.g., thioureidoimidazoline [27] and ultrafine bubbles [28], 76 water chemistry [16], [18] e.g., oxygen content [29], pH [30], and maintenance strategies [25] 77 e.g., pipe geometry [31], water flow. Among these methods, metal formulation and chemical 78 inhibitors are the most effective treatments used to prevent the FAC [32]. Carbon steels with 79 Cr-enriched phase display excellent corrosion resistance against FAC [30]. Cr in carbon steel inhibits the diffusion of Fe in the oxide film through the formation of a FeCr₂O₄ [16]. An 80 81 example of chemical inhibitors is the usage of hydrazine (N₂H₄) and ammonia (NH₃) or 82 ethanolamine (C₂H₇NO) that act as oxygen scavengers to maintain the stability of protective oxide [33]. The implementation of these methods may minimize the catastrophic failures of 83 84 pipes while improving operations and safety reliability. Several reviews and book chapters 85 have summarized FAC in NPPs, for instance, the work of Gipon and Trevin [34], which 86 provided a detailed account of EDF's operational experience and the BRT-CICERO modeling 87 framework. Although many reviews have provided useful information about FAC mechanisms 88 and management practices, these reviews mostly looked at traditional plant-level codes and 89 maintenance strategies. In contrast, this review offers a contemporary synthesis that 90 amalgamates predictive models (including CFD and ML approaches), advanced experimental 91 autoclave methods, and recent material/microstructural insights, thereby extending the scope 92 beyond earlier works.

2. Mechanism of FAC

93

94

95

96

97

2.1 Electrochemical basis of FAC

The mechanism of FAC is fundamentally rooted in the electrochemical interactions between the metal surface and the flowing aqueous environment [35], which lead to the destabilization and dissolution of protective oxide films. Basically, the oxide film on the surface of carbon steel acts as a barrier layer against corrosion. Figure 1 summarizes the reactions that occur during the formation of an oxide film on the surface of carbon steel. This process includes an oxygen-diffusion-limited step (step 2), the partial formation of the film (step 3), the thickening of the film (step 3), and the complete formation of the magnetite film (step 4). Step 3 does not take place without the occurrence of the Schikorr reaction, which governs the transformation of Fe(OH)₂ to Fe₃O₄ [36].

FAC is ascribed to the dissolution of the Fe₃O₄ on the surface of carbon steel under water flow conditions. Figure 2 presents a comprehensive schematic of the FAC mechanism, highlighting the four key stages: (1) iron oxidation due to high temperature and high pressure, (2) diffusion of ferrous species through the oxide, (3) formation and dissolution of magnetite, and (4) transport of ferrous ions into the bulk flow [35]. These schematics illustrate specific processes: in Figure 2(a) shows ferrous species diffusion through the oxide; in Figure 2(b), the removal of Fe(OH)⁺ and Fe²⁺ across the boundary layer is highlighted; Figure 2(c) presents the stepwise electrochemical and mass transfer fluxes; and Figure 2(d) provides CT images of welded joints (P22-SA106 interface), confirming flow-induced wall thinning. There are mainly two types of FAC, including single-phase and two-phase FAC, as shown in Figure 3. Figure 3 compares single-phase FAC, in which water flow increases the dissolution of Fe₃O₄, to two-phase FAC, where steam water vapor droplets remove magnetite via impaction and high shear turbulence [37], [38]. Figure 3(I) shows hydrodynamic control of Fe²⁺ release (measured via hydrocal tests); Figure 3(II) illustrates wall-thinning morphologies in single-phase vs. twophase regimes (e.g., tiger-striping and chevron marks); and Figure 3(III) compares the mechanistic role of impurities and flow hydrodynamics.

120 Fe
$$\rightarrow$$
 Fe²⁺ + 2e⁻ (1)

121 In aqueous environments, Fe²⁺ reacts with hydroxide ions to form ferrous hydroxide:

122
$$Fe^{2+} + 20H^{-} \rightarrow Fe(0H)_{2}$$
 (2)

123 Then, ferrous hydroxide undergoes the Schikorr reaction to form magnetite:

$$124 3Fe(OH)_2 \to Fe_3O_4 + H_2 + 2H_2O (3)$$

Dissolution of the Fe₃O₄ layer is determined by the solubility of the oxide on the surface of

metals. Reaction can be explained as:

98

99

100

101

102

103

104

105

106

107

108

109

110

111

112

113

114

115

116

117

118

119

127
$$Fe_3O_4 + 4H^+ + 2e^- \rightarrow 3Fe^{2+} + 40H^-$$
 (4)

Low-velocity conditions can be maintained by a relatively protective oxide film through

129 ferrous hydroxide [Equation (2)] and magnetite formation [Equation (3)]. Under turbulent flow

conditions, magnetite dissolution [Equation (4)] then becomes the rate-limiting step in the progression of FAC. The hydrodynamic stress increases mass transfer by reducing the thickness of the diffusion boundary layer, such that Fe ²⁺ ions generated at the oxide/water interface are swept quickly into the bulk flow. This prevents local saturation, ensures a large concentration gradient, and hence continual dissolution of the Fe₃O₄ layer. As shown by Khunphakdee and Chalermsinsuwan [35], the FAC rate can be characterized as a function of the Reynolds number, the Schmidt number, and the Sherwood number, which are used to describe the turbulent flow of the fluid and the efficiency of the mass transfer coefficient. In this way, [Equation (4)] directly explains why high-velocity and disturbed flows such as downstream elbows or orifices accelerate FAC damage by driving faster removal of soluble iron species from the magnetite layer.

130

131

132

133

134

135

136

137

138

139

140

141

142

143

144

145

146

147

148

149

150

151

152

153

154

155

156

157

158

159

160

161

162

163

The continuous dissolution of Fe₃O₄ into the bulk results in the acceleration of the FAC rate of metals [35]. Figure 4 illustrates the detailed nanoscale analysis of the ferritic steel microstructure affected by FAC. In Figure 4(a), a bright-field transmission electron microscopy (BE-TEM) image reveals the presence of ferrite nanocrystals embedded with Fe₃C and Fe₃O₄ phases, as highlighted by red arrows. Elemental energy-dispersive X-ray spectroscopy (EDX) mapping confirms the spatial distribution of Fe, O, and Cr. Figure 4(b) provides the corresponding selected area electron diffraction (SAED) pattern, identifying diffraction rings for ferrite and Fe₃C. Figure 4(c-f) presents high-resolution imaging of dislocations and subgrain boundaries. Subfigure (c) shows dislocation accumulation, while (d) and (f) confirm the coexistence of ferrite and Fe₃C phases. The fast fourier transformation (FFT) patterns in Figure 4(e) and (g) further validate crystallographic orientations and angular misorientation (7.5°-8.4°), indicating local lattice strain. Figure 4(h-j) focus on region 2 in (a), where dislocation-rich and dislocation-free zones are evident. The high-resolution transmission electron microscopy (HR-TEM) image in Figure 4(j) highlights a small-angle boundary (~2.82°), suggesting localized deformation mechanism [39]. Figure 5 further elucidates the microstructural features associated with FAC-affected ferritic steel. BE-TEM image reveals that the ferrite matrix contains nanocrystalline grains interspersed with Fe₃C and Fe₃O₄ phases, as verified by elemental EDX mapping of Fe, O, and Cr. The corresponding SAED patterns confirm the presence of both ferrite and Fe₃C, while FFT analyses reveal notable angular misorientations ranging between 7.5° and 8.4°, indicating lattice distortions. Dislocation structures and sub-grain boundaries are prominent, especially in regions containing lamellar pearlite. HRTEM image highlights localized deformation, with small-angle grain boundaries (~2.82°), suggesting stress accommodation mechanisms that may contribute to oxide layer

destabilization. These nanoscale features underscore the critical role of grain boundary character, phase composition, and localized strain in accelerating FAC degradation [39].

2.2 Mass transfer mechanism of FAC

Mass transfer is considered the transfer of molecules/ ions from a site with high concentration to the other site with low concentration [40]. Mass transfer is driven by the concentration difference [40], [41]. As shown in Figure 6, localized defects such as depressions and weld reinforcements significantly distort flow patterns, creating micro-turbulent zones that promote selective corrosion and enhance mass transfer rates. This is widely recognized for the case of exposing carbon steel and low alloy steel to flowing water or wet steam [41]. Diffusion of the ferrous species such as Fe(OH)₂ through the outer layer on carbon steel and low alloy steel is driven by the concentration diffusion [36], [41], [42]. High flow velocity and turbulence enhance the mass transfer rate of ferrous ions from the outer oxide layer into the bulk fluid [43], particularly at tees, bends, and elbows [40], [42]. This maintains a steep concentration gradient, promoting sustained dissolution [44]. The dissolution initiates at the oxide-metal interface, where ferrous ions (Fe²⁺ and FeOH⁺) are generated and then diffuse across the oxide layer, eventually being removed by the turbulent bulk water.

There is a relationship between flow velocity, FAC rate, and electrochemical potential (ECP) [45], [46], [47]. FAC rate of carbon steel measured at 140 °C in neutral water showed that the increase in flow velocity reduced boundary layer thickness, enhancing both the anodic and cathodic current density [46]. With increasing the flow velocity, the ECP of carbon steel obtained from the potentiodynamic polarization curve shifted to more negative potential due to the passivity breakdown of the oxide layer [45], [46].

3. Factors influencing FAC

FAC is controlled by the interplay of multiple parameters, mainly categorized into environmental conditions [48], hydrodynamic influence [49], and material properties [50]. These factors collectively control the formation and stability of oxide films [51], modify electrochemical kinetics [52], and contribute to surface stress and metal degradation. Environmental influences, such as temperature [36], [53], pH [35], and dissolved oxygen [29], are particularly critical in initiating and sustaining FAC processes. Variations in these conditions can alter the thermodynamic stability of oxide layers, thereby weakening their protective function. In FAC-prone systems, changes in water chemistry may significantly influence the corrosion rate and its propagation pattern.

3.1 Environmental factors

Three major environmental factors have been found to affect FAC rates of metals, including temperature, pH, and oxygen concentration (Table 1) [54], [36], [30], [29]. As illustrated in Figure 8 [46], these parameters, when coupled with other influencing variables such as flow pattern and chromium content, define a high FAC risk zone. The diagram emphasizes that accurate evaluation of corrosion susceptibility to FAC requires considering multiple interacting variables. The solubility of magnetite peaks between 150 and 180°C, thereby accelerating FAC rates. Similarly, maintaining water chemistry with a pH > 9 and a low dissolved oxygen level is essential for stabilizing magnetite layers and reducing oxide dissolution. This is one of the most effective strategies for controlling FAC in reactor coolant systems [54]. Similarly, lower oxygen concentrations increase electrochemical activity, which promotes the progression of FAC.

3.2 Hydrodynamic parameters

Hydrodynamic parameters play a central role in governing the onset and progression of FAC. Key variables such as flow velocity, Reynolds number, turbulence intensity, and wall shear stress insignificantly influence both the mass transport of ions and the mechanical removal of protective oxide layers. Elevated flow velocities and intensified turbulence reduce the boundary layer thickness at the metal–fluid interface, thereby enhancing the transport of ferrous ions and promoting higher corrosion rates [14], [46], [55], [56]. As illustrated in Figure 9, regions of elevated wall shear stress coincide with lower charge transfer resistance (R_{ct}) and higher corrosion current density (i_{corr}), confirming that turbulence enhances oxide film dissolution. Localized eddies and flow separation at bends or elbows intensify wall shear, thinning the diffusion boundary layer. This hydrodynamic amplification of electrochemical reactions explains why FAC damage is consistently most severe at high-turbulence locations such as elbows and downstream of orifices.

Experimental studies under controlled conditions have consistently confirmed the sensitivity of FAC to variations in hydrodynamics. Disturbances downstream piping features such as bends, elbows, orifices, and T-junctions generate complex flow fields that amplify turbulence and induce localized corrosion [47]. Various experimental loop systems have been developed for evaluating the FAC rate of metals. Figure 10 presents a comparative overview of representative FAC test setups, highlighting configurations tailored for specific conditions such as High-pressure flow loop (HPFL), high temperature, multiphase flow, and

electrochemical monitoring. These systems integrate components such as centrifugal pumps, CO₂ injection, array electrodes, and data acquisition instrumentation to simulate and study FAC under controlled yet realistic operating parameters. Their design enables researchers to examine the effects of flow-induced shear, dissolved oxygen, temperature, and geometry on corrosion behavior, thereby supporting the development of predictive models and mitigation strategies. Figure 11 further demonstrates how the severity of corrosion varies depending on the flow geometry and local hydrodynamics within these test loops. Electrochemical impedance spectroscopy (EIS) data presented in Figure 11 are obtained from the HPFL system shown in Figure 10(a). In this loop system, the test section was designed to evaluate the FAC rate at 16 sites. As shown in Figure 11(a), electrodes 3 and 4 exhibited the lowest corrosion resistance as based on the semicircle diameters of Nyquist plots, while electrodes 1 and 2 showed comparatively higher impedance, indicating better protection against FAC. Madasamy et al. [14] reported that corrosion rates at pipe bends were more than twice those observed in straight sections, primarily due to increased turbulence and flow separation. Similarly, Yoneda et al. [46] demonstrated that while lower temperatures generally reduce FAC severity, elevated velocities maintain high corrosion rates even under cooler conditions, confirming the dominant influence of flow velocity. Figure 12 illustrates how the surface morphology of carbon steel is significantly affected by variations in chloride concentration, pH, and flow velocity. Distinct corrosion scale structures—ranging from single-layer films to complex two-layered and wrinkled formations—demonstrate how water chemistry and hydrodynamic forces shape FAC development under different conditions [43] Figure 13 complements this by highlighting the redistribution of two-phase flow and the resulting erosion features downstream of orifices with varying geometric ratios. These flow-induced disturbances reveal localized zones of intensified degradation, reinforcing the critical interplay between fluid dynamics and corrosion processes in FAC [17]. Figure 9 illustrates the redistribution of two-phase flow downstream of orifices at different diameter ratios ($d_0/D = 0.25, 0.5, 0.74$), ($d_0/D = 0.25, 0.5, 0.74$), ($d_0/D = 0.25, 0.5, 0.74$) 0.74) and vapor qualities (x=0.001-0.003), (x = 0.001-0.003), (x=0.001-0.003). At low vapor quality, the flow is dominated by dispersed bubbles and a relatively continuous liquid phase, ensuring substantial wall wetting. When the vapor quality increases, vapor pockets grow and join together, pushing the liquid film away from the pipe wall. This effect becomes more pronounced at higher orifice ratios, where large gas structures and churn-like flow patterns develop, significantly reducing the liquid-wall contact area. This phenomenon directly explains the observed suppression of FAC wear rates in high void-fraction conditions. These findings underscore how hydrodynamic and chemical environments contribute to real-world

230

231

232

233

234

235

236

237

238

239

240

241

242

243

244

245

246

247

248

249

250

251

252

253

254

255

256

257

258

259

260

261

262

FAC failures, which have historically caused significant safety concerns and operational disruptions. Table 2 provides a summary of notable FAC-related pipe rupture incidents reported in NPPs.

Additional investigations have further explored the impact of orifices and sudden flow contractions, which produce zones of peak turbulence and fluctuating wall shear stress [47]. These conditions can accelerate the oxide film dissolution by enhancing ion exchange at the metal surface. Utanohara et al. [57] and Ahmad et al. [58] highlighted that the maximum FAC thinning typically occurs one to two pipe diameters downstream of an orifice, wherein turbulent intensity is greatest. Furthermore, a strong linear correlation was observed between wall shear stress and FAC rate, supporting the use of predictive computational methods such as large eddy simulations (LES) for identifying high-risk regions.

Recent advances in experimental and modeling techniques have enabled a more detailed examination of hydrodynamic effects on FAC. Studies using high-resolution particle image velocimetry (PIV) and electrochemical probes have demonstrated that local wall shear stress governs mass transfer coefficients and, in turn, corrosion kinetics [59], [60]. CFD simulations and electrochemical measurements—such as those using array electrodes—have been instrumental in identifying regions of high turbulent kinetic energy and wall thinning in elbow sections of carbon steel pipelines [61], [62], [63]. Moreover, vorticity and eddy formation have been proposed as indicators for FAC susceptibility [64]. Coupled fluid-structure interaction (FSI) analyses have also shown that cyclic flow disturbances can induce mechanical fatigue, exacerbating material degradation in critical piping systems [65].

Collectively, these studies highlight the critical importance of flow dynamics in controlling FAC rates. Each factor, including flow velocity, turbulence intensity, Reynolds number, and wall shear stress, synergistically contributes to the dissociation of protective oxide layers on surfaces within piping systems.

3.3 Material composition

Optimizing alloy composition is a fundamental strategy for mitigating FAC in high-temperature water systems [35]. Chromium-rich alloys, such as 316 stainless steel, have demonstrated superior resistance to FAC due to the formation of a stable chromium-oxide layer, acting as a barrier against turbulent flow conditions [66]. Corrosion rates of 316 stainless steel and 304 stainless steel in similar environments were 0.71 μ m/year and 2.6 μ m/year, respectively [67]. Mo in 316 stainless steels can not only contribute to the stability of passive

films, but it can also improve the resistance against pitting and crevice corrosion in aggressive environments such as molten FLiBe salt [68].

296

297

298

299

300

301

302

303

304

305

306

307

308

309

310

311

312

313

314

315

316

317

318

319

320

321

322

323

324

325

326

327

328

These findings [67], [68] underscore the importance of deliberate alloy design, where the incorporation of specific elements like Cr and Mo can significantly enhance the corrosion resistance of structural materials exposed to FAC-prone conditions. Figure 14 illustrates the progressive development of a protective bi-layer oxide structure in Cr-containing low alloy steels, demonstrating how Cr promotes the formation of stable oxide layers under hightemperature flowing water [23]. Chromium (Cr) additions are widely considered beneficial for mitigating FAC in low-alloy steels, but the literature shows divergent findings. Chromium (Cr) additions are widely considered beneficial for mitigating FAC in low-alloy steels, but the literature shows divergent findings. Kim et al. [23] found that Cr content and FAC resistance were strongly positively correlated: PWR-simulation experiments at 150 °C in water indicated that steel containing more Cr (approximately 4 wt%) formed Cr-enriched oxide layers and experienced much lower rates of FAC. In contrast, Wang et al. [69] reported that under extreme flow and wall shear stress conditions (212 Pa) in wet gas, carbon steel could not sustain an intact FeCO₃ corrosion film, whereas 3 wt% Cr steel formed a mixed Cr(OH)₃ + FeCO₃ film that remained protective. This inconsistency could possibly be explained by variations in test environments (e.g., high-temperature, deoxygenated water in Kim [23] vs. high-flow wet gas in Wang et al. [69]), and perhaps even by effects related to a Cr threshold—small Cr additions might be required to reach a certain level of activity to stabilize and form a protective Cr oxide. Moreover, the two studies also employed different methods of oxide characterization (Kim et al. [23] performed detailed analyses using TEM/EDS and X-ray to demonstrate Cr substitution in magnetite and its passivating effect, whereas Wang et al. [69] examined film composition under high shear, which showed that a mixed film can survive where pure FeCO₃ fails). These contrasting results highlight a broader research gap in understanding how Cr and other alloying elements interact with hydrodynamic and chemical conditions to influence FAC. Standardized, systematic studies are needed to clarify these interactions and guide the selection of alloy compositions for FAC resistance

Different classes of steel are applied depending on the reactor design:

 Chromium Steels: Martensitic 9-12% chromium steels offer exceptional hightemperature strength, creep rupture resistance, and irradiation performance, making them suitable for advanced reactors [70] Figure 15 illustrates how Cr and Mo addition alter the oxide layer structure, with EDS analysis confirming enhanced stability and

- elemental distribution at the interface [71]. Their cost-effectiveness compared to nickel-based alloys further promotes their use in non-nuclear components like supercritical steam turbines [72], [73]. Figure 16 illustrates how varying Cr content influences oxide layer composition and corrosion potential, further supporting the critical role of Cr in enhancing FAC resistance in structural steels [30], [74].
 - Austenitic Stainless Steels: Types 316, 304, and 15/15 are preferred for light water reactor interiors owing to their corrosion resistance and mechanical properties at elevated temperatures. To improve yield strength, austenitic steels are often cold worked [75]. Their metallurgical behavior, thermal fatigue resistance, and SCC performance under reactor conditions have been extensively investigated [75], [76], [77], [78], [79], [80].

Further studies highlighted critical challenges:

- Thermal aging in Z₃CN₂₀-09M cast stainless steel increased hardness by 20%, affecting long-term performance [81].
- Fretting wear in steam generator tubes caused localized oxide thinning and accelerated corrosion [82].
- Chromium depletion in sodium-cooled fast reactors reduced SCC resistance by 15%
 [83].
 - Borated austenitic steels enhanced neutron absorption but became prone to corrosion-assisted cracking [84].
 - Containment liner degradation in chloride environments reduced structural load-bearing capacity by up to 25% [85], [86].
- Post-accident hydrogen evolution risks were associated with aluminum alloys in alkaline sump water [87].
 - Despite extensive studies on chemistry, hydrodynamics, and alloying elements, important gaps remain. Environmental models often neglect transient effects and radiation-driven radiolysis [35], [36], while hydrodynamic correlations may not hold under multiphase turbulence or FSI conditions [47], [57], [58]. Similarly, Cr/Mo/Cu alloying looks promising [23], [30], [74], but there are still no standards for threshold levels, long-term stability, or radiation-assisted degradation. These gaps highlight the necessity for systematic, reactor-relevant investigations that connect environmental factors, flow dynamics, and material characteristics to oxide stability and FAC resistance.

4. Theoretical models for FAC prediction

4.1 Sánchez-Caldera model

Scientists created the Sánchez-Caldera model as a semi-empirical system to calculate FAC rates through iron ion transport from steel surfaces to flowing water [88]. This model unifies hydrodynamic aspects of velocity and flow turbulence with electrochemical elements from oxygen concentration and temperature [89], [90]. The model establishes mass transfer control of the FAC process through ferrous ion actions and uses dimensionless factors from Reynolds and Schmidt numbers to derive its mass transfer coefficient [91]. As a result, it has been foundational in advancing the understanding of FAC mechanisms and has significantly influenced the development of subsequent predictive tools and methodologies [92], [93]. The FAC thinning rate (r) in this model is expressed as [94]:

$$372 r = k_m \cdot C_{Fe} (5)$$

where $k_{\rm m}$: mass transfer coefficient and $C_{\rm Fe}$: the solubility of ferrous ions at the metal-water interface. The model is particularly useful for predicting FAC in carbon steel pipes under single-phase flow conditions in the secondary circuits of nuclear power plants.

In summary, the Sanchez-Caldera model has the advantages of being rather simple yet encompasses several of the most important factors influencing FAC. For this reason, it has been widely used as a basis for software prediction tools of the wall thinning rates due to FAC. However, the model does not take into account the bilayer structure of the oxide film, as well as the possibility of an alteration of the mechanical and electrochemical properties of the surface layer at the oxide/electrolyte interface. In addition, it does not account for the two-layer structure of the oxide film on steel or changes in the properties of oxide at the metal-water interface. This oversimplification of the FAC mechanism means the model is mainly valid for single-phase flows, and this model may not capture complex turbulent flow dynamics in more challenging conditions [90].

4.2 CEGB model

The Central Electricity Generating Board (CEGB) became one of the first extensive attempts to predict feedwater system FAC behavior. The model applies mass transfer principles in combination with several operational parameters, including pH and dissolved oxygen levels, together with temperature and flow velocity [90]. The CEGB model demonstrates excellent calibration properties through its utilization of operational data from British power plants for making reliable empirical predictions across different service environments [90]. Unlike the

Sánchez-Caldera model, the CEGB model gives greater weight to chemical factors, especially the influence of water chemistry on protective oxide film stability [95]. The model separates different flow conditions, including single-phase and two-phase, while it shows how oxide solubility depends on pH and temperature values [96]. A key limitation is that the original CEGB model neglects the effect of surface roughness on corrosion rates. In other words, it assumes a simplified flow behavior which may become outdated when applied beyond the boundary conditions of its original dataset, reducing its predictive reliability under modern or differing plant conditions [94].

4.3 Other predictive models

In addition to the classical models, various modern approaches have been proposed to enhance FAC prediction accuracy. These include:

- **Ducreux Model** [97]: The Ducreux Model applies widely across France since it combines FAC rate estimation with the analysis of materials through Cr content and other alloying factors. The model focuses on how oxide film stability, together with its formation conditions, influences various flow conditions in plants. This validated model works with different steel materials to analyze alloying effects on reducing FAC issues.
 - **CFD-Based Models:** CFD techniques enable detailed spatial analysis of turbulent flow structures and wall shear stress distributions [98], [99], [100]. By integrating CFD outputs with mass transfer correlations and corrosion kinetics, these models offer highresolution predictions of localized thinning in critical regions. For example, one study highlighted the utility of CFD in simulating flow in 45° elbows under PWR and boiling water reactor (BWR) conditions, noting the novelty of the setup but lacking comparative validation with experimental data [101]. Other CFD-based approaches aimed to simulate FAC in complex geometries such as bifurcations and nozzles, though some efforts were limited by insufficient validation or by neglecting surface roughness effects [102]. Efforts to model FAC in Mihama conditions using CFD faced similar challenges, particularly the absence of comparison with empirical results and the exclusion of roughness influences [103]. In contrast, more comprehensive simulations addressed the FAC behavior in CANDU feeder pipes, incorporating roughness evolution and geometry-induced interaction effects to better mirror actual degradation patterns [104]. Another significant contribution underscored that wall shear stress and mass transfer coefficients may not correlate directly in sudden expansion zones,

- indicating the importance of local flow features in FAC prediction [105], as shown in Figure 7.
- Data-Driven and Machine Learning Models: Recent advancements include the use of artificial neural networks (ANN) and regression models trained on plant operating data [106]. These models aim to overcome the complexity of multifactorial influences in FAC by identifying non-linear patterns across temperature, pH, material, and flow velocity variables [107]. A range of experimental and modeling efforts have been undertaken to study FAC under controlled conditions, focusing on material behavior, hydrodynamics, and environmental influences. Table 3 summarizes key findings from selected studies, outlining the methodology, type of steel, testing sections, and observed outcomes. However, such ML methods are able to learn complex variable interactions and achieve higher predictive accuracy, their non-interpretability is currently a limitation in implementing them in safety-critical, regulated environments [108]. These black-box models do not readily explain why a prediction is made [108]. To address this gap, recent efforts apply explainability techniques like SHapley Additive exPlanations (SHAP) - a post-hoc analysis method that quantifies each input's contribution to the prediction – thereby illuminating the decision process of the model [90]. By using tools such as SHAP to identify key features and nonlinear interactions driving FAC predictions, researchers are able to make ML models more transparent. Moving forward, data-model-driven approaches will be important for developing adaptive, real-time control of FAC that is both accurate and regulatory-ready [90], [108]. CFD models offer comprehensive flow predictions [98], [99], [100], [101]. However, CFD models frequently lack validation in irradiation-relevant chemistries and rarely incorporate roughness/oxide evolution [103], [104]. Simplified WSS-mass transfer assumptions frequently fail in recirculating zones [105], whereas ML approaches, despite their accuracy [106], [107], [108], are constrained by issues of interpretability and regulatory preparedness. For future progress, researchers should combine CFD/kinetics with ML.

5. Corrosion testing techniques for FAC

5.1 Vibration-based diagnosis of FAC

426

427

428

429

430

431

432

433

434

435

436

437

438

439

440

441

442

443

444

445

446447

448

449

450

451

452

453

454

455

456

457

458

Vibration-based analysis is used to simulate realistic operating conditions, and it is also used to assess the corrosion behavior of FAC of metals. Chae et al. [109] investigated the feasibility of employing vibration signal analysis to diagnose pipe wall thinning due to FAC. Vibration

data were captured using three-axis accelerometers operating at a measurement frequency of 20 kHz. FAC-induced thinning of carbon steel was monitored under operational loop conditions (pH = 4, pressure = 20 bar, temperature = 120°C). The results revealed that in artificially thinned pipes, vibration modes exhibited distinct frequency peaks that shifted systematically with increasing thickness loss. Further reinforcing this approach, Chung et al. [110] studied the modal characteristics of curved cylindrical structures such as elbows, which exhibit non-uniform thickness distributions and complex mode shapes due to their fabrication processes. Their research combined numerical simulation with multiple reference impact testing (MRIT) to analyze artificially thinned carbon steel elbows under various thinning states. Chung et al. [110] found that the natural frequencies of specific shapes decreased linearly with increasing wall loss. Moreover, the study proposed a cost-effective thinning estimation technique by comparing single-point frequency response function (FRF) measurements with MRIT results, highlighting a practical approach to monitor FAC-related thinning in nuclear piping systems [110].

These findings in studies [109], [110] highlighted the challenges of detecting FAC progression through vibration analysis in realistic scenarios. The subtle nature of FAC-induced degradation necessitated more advanced signal processing techniques. Consequently, the study proposed incorporating ML models in future work to improve the classification accuracy of vibration-based corrosion diagnosis under operational conditions.

The vibration signals of the FAC-induced through-wall loss of pipe wall thickness are sometimes manifested through only minimal variations. This might be difficult to distinguish from normal operational vibration and noise with conventional analysis techniques [108]. In other studies wherein FAC-induced thinning occurs in pipes, vibration spectra were assessed, and the indications of such thinning can be easily identified in any pipe other than those with FAC-induced thinning, with conventional frequency analysis [109]. This finding implies that FAC degradation signatures are very subtle, demanding more advanced signal processing for detection. To address this, ML algorithms such as Support Vector Machine (SVM), Convolutional Neural Network (CNN), and Long Short-Term Memory (LSTM) were applied to vibration recording data for training and analysis [109]. This approach substantially improved the accuracy of defect detection. Among these methods, the deep learning model based on LSTM achieved the best performance, reaching nearly perfect accuracy (96%) in identifying wall thinning as small as 0.4 mm from vibration signals, which is not achievable through generic thresholding techniques. This is clear evidence that ML is required to identify the complex patterns and frequency shifts. Overall, leveraging advanced signal processing and

ML techniques allows vibration-based monitoring systems to pick up early, small changes in structural response that would otherwise go unnoticed [108]. By incorporating ML models into vibration diagnostics, one can significantly enhance the detection and classification accuracy for FAC-induced damage under real operating conditions, addressing the challenges documented in studies [109] and [110].

Additional research supports this approach. For example, Kim et al. [111] analyzed how localized thinning affects the collapse behavior of pipe elbows under combined loads, reinforcing the significance of monitoring structural responses to corrosion-induced degradation. Similarly, Oh et al. [112] developed a high-temperature ultrasonic waveguide system for online wall-thickness monitoring, successfully detecting gradual thinning caused by FAC in thermal-hydraulic loop environments. The combination of vibration-based systems with hybrid methods is becoming increasingly important for FAC risk management in NPP infrastructure, where automated non-intrusive condition monitoring becomes possible.

5.2 Stirred autoclave

One of the most widely adopted methods for assessing corrosion resistance of metallic materials is using stirred autoclave systems [113]. In these setups, metal coupons are submerged in corrosive medium while an impeller stirs the solution to maintain homogeneity, thereby mimicking the dynamic chemical environment encountered in operational facilities. Tomoe et al. [113] investigated the inhibition efficiency of amines and carboxylates in a Hastelloy C-276-lined stirred autoclave under a CO₂-saturated environment. 13% Cr steel was exposed to 135°C and 150°C, and pressures of 448 psi and 479 psi. Ding et al. [114] employed a two-stirred autoclave system to examine the mitigation of CO₂ corrosion on API 5L X65 carbon steel using a diethylenetriamine tall oil fatty acid imidazoline-type inhibitor. Experiments were conducted at 120°C and 150°C under CO₂-saturated 1 wt.% NaCl solution, highlighting the role of optimized inhibitor chemistry. Hoshowski et al. [115] further explored the challenges of inhibiting corrosion at elevated temperatures ranging from 120 °C to 177 °C in a sour environment containing CO₂ and H₂S. Their findings revealed the limitations of traditional imidazoline-based inhibitors above 150°C, prompting the development of advanced formulations capable of maintaining effectiveness at up to 175°C. Additional studies have reinforced these findings by evaluating CO₂/H₂S corrosion inhibition efficiency of thioglycolic acid [116], bis-imidazoline compounds [117], and the mechanistic correlations of carbon steel corrosion in CO₂-saturated brines [118]. Other reviews emphasize environmentally sustainable inhibitor chemistries [119], [120], [121]. Despite their widespread usage, stirred autoclaves

present limitations in simulating high-shear dynamic flows, which are common in real pipeline and reactor environments. To address this, specialized rotating electrode autoclaves have been developed [122].

5.3 Rotating cylinder electrode (RCE) and rotating disk electrode (RDE) autoclaves

RCE and RDE autoclaves enhance mass transfer rates and provide more uniform reactant distribution by rotating the electrode (samples) during testing [123]. In RCE systems, cylindrical coupons are mounted on a rotating shaft, enabling better simulation of flowenhanced mass transfer conditions. RDE systems, in contrast, use flat disk-shaped electrodes where the flow remains largely laminar, making them less suitable for replicating turbulent flow profiles observed in practical piping systems. Recent work has mapped wall shear stress distributions in rotating cage and RCE systems [124], while other studies evaluated inhibitor performance in CO₂-saturated solutions with synergistic additives such as L-cysteine [125]. Although RCE and RDE devices enhance mass transport phenomena compared to stirred autoclaves, both autoclaves still face challenges in accurately reproducing the complex, turbulent flows typically associated with FAC environments [126], [127].

5.4 Jet impingement autoclave

Jet impingement autoclaves are specifically designed to simulate high-shear, high-turbulence flow conditions, closely mimicking environments like the annular mist flow regime encountered in pipelines [128], [129]. This configuration consists of an autoclave system coupled with an external circulation loop where fluid jets impinge directly onto metal specimens, generating high local shear stresses. Palencsár et al. [130] utilized jet impingement autoclave to investigate the corrosion inhibition of *oleic imidazoline* and *cocoalkyl quat* for API X65 carbon steel under CO₂-rich, and high-temperature conditions. Another system utilized AISI 1018 steel under 93°C and 80 psi, simulating 0.0145 psi shear stress (~100 Pa) to evaluate the passive film breakdown under high-velocity multiphase conditions [131]. Moreover, under similar alloy and pressure conditions, a test loop incorporating electrochemical linear polarization resistance (LPR) and EIS demonstrated that shear stress >200 Pa could significantly reduce inhibitor efficiency due to mechanical disruption of protective layers [132]. Complementary investigations confirm that protective iron carbonate scales play a critical role in inhibitor stability under jet impingement [133], [134].

5.5 Rotating cage (RC) autoclave

556

557

558

559

560

561

562

563

564

565

566

567

568

569

570

571

572

573

574

575

576

577

578

579

580

581

582

583

584

585

586

587

588

Rotating Cage (RC) autoclaves offer another robust platform for simulating dynamic flow conditions and high turbulence [135]. In an RC autoclave, metal coupons are mounted onto a rotating cage made of non-conductive materials like Teflon to prevent galvanic effects. The cage is rotated at controlled speeds to replicate a range of flow velocities. For instance, Laurent et al. [136] utilized RC autoclaves with API 5L X65 carbon steel to study the effect of calcium carbonate scale formation on the efficiency of a proprietary amido-imidazoline-based corrosion inhibitor at temperatures exceeding 121°C. In another study, Ramachandran et al. [137] conducted high shear testing at 232°C and 1500 psi CO₂ pressure using AISI 1018 steel coupons. The researchers evaluated the performance of three types of corrosion inhibitors including cyclic amines, amido-imidazolines, and quaternary ammonium imidazolines under 2000 rpm rotation speed, simulating a wall shear stress of approximately 6.65 m/s. Their findings confirmed that the inhibitor performance significantly varies with shear intensity, making RC autoclaves highly valuable for screening inhibitors under extreme dynamic conditions. Recent journal contribution further emphasize the RC autoclave utility in corrosion inhibition study [138], supported by mechanistic insights into corrosion under CO₂/H₂S environments [139], [140]. Although corrosion testing platforms—from stirred to RC autoclaves—have advanced FAC research, they remain limited by short test durations, absence of irradiation/radiolysis effects, and incomplete replication of multiphase turbulence [113], [140]. Although inhibitors lose effectiveness above about 200 Pa shear, as confirmed by jetimpingement and RC studies [132], it is unclear how long corrosion inhibitors will last under continuous flow. Future development requires integrating CFD/ML validation under reactorrelevant chemistries with high-shear autoclaves and in-situ electrochemical diagnostics.

Overall, while laboratory methods such as stirred autoclaves and rotating cylinder electrodes enable controlled corrosion testing, significant limitations persist, particularly in replicating the high-shear turbulence and complex flow profiles found in real-world pipelines. The comparative summary in Table 4 highlights how differences in Reynolds number and flow dynamics lead to discrepancies in simulation fidelity for each method.

6. FAC control and mitigation strategies

6.1 Metal formulation

Alloying elements, particularly Cr [53], [141,142], Mo [23], [143], and copper (Cu) [144,145], modify the properties of the protective oxide layer formed on the surface of the steel, thus determining stability, compactness, and resistance to dissolution under flow

conditions. Numerous experimental studies have demonstrated that the addition of Cr significantly enhances the resistance of low-alloy steels to FAC by improving oxide film characteristics.

Dooley and Chexal [53] reported that even minor Cr additions (~0.1–0.3 wt%) can drastically reduce FAC rates in nuclear and fossil plant components. Cr stabilizes the Fe₃O₄ layer by reducing its solubility and promoting the formation of Cr-enriched protective films. Severe surface degradation is typically observed in Cr-deficient alloys, characterized by rough, porous oxide structures, while alloys with progressively higher Cr contents display smoother and more intact surfaces, indicating improved FAC resistance [23].

In-depth microstructural analysis further clarifies the critical role of Cr content in enhancing FAC resistance. As shown in Figure 17, Kim et al. [23] used TEM and SAED to study the oxide layers formed on different Cr-containing steels, including P22 (2.09Cr–0.95Mo), FRA 1 (2.25Cr–1Mo), FRA 2 (3.2Cr–0.5Mo), and MFRA (4.2Cr). Results revealed that the outer oxide layer of the film on these alloys is predominantly amorphous and Cr-rich, while the inner oxide layers consist of crystalline Fe₃O₄ with partial substitution of Cr into the spinel lattice. The amorphous Cr-rich outer layer serves as an effective barrier to ionic diffusion, thereby reducing the solubility and mobility of iron ions and ultimately improving corrosion resistance. This protective behavior is especially evident at higher Cr contents and mild alkaline pH levels, as illustrated in the schematic and time-of-flight secondary ion mass spectrometry (ToF-SIMS) depth profiles (Figure 17). These findings reinforce the importance of both chromium alloying and water chemistry in mitigating FAC.

Xu et al. [146] investigated the effect of Cr content on steel corrosion performance in CO₂-saturated environments. Using in-situ Raman spectroscopy, Xu et al. [146] found that the addition of 3% Cr into steels induced the formation of Cr(OH)₃, which significantly improved corrosion resistance. Low-Cr steels suffered from localized corrosion, while high-Cr steels maintained smooth and intact surfaces. Raman spectra confirmed the presence of Cr-rich compounds on high-Cr samples, while low-Cr steels predominantly formed porous iron oxides [146].

Similarly, Jiang et al. studied the impact of Cr on FAC behavior in saline NaCl environments using surface analysis techniques [74]. Their work demonstrated that Cr additions modified the rust layer, forming dense Cr-goethite phases that offered excellent protection against FAC. Moreover, X-ray photoelectron spectroscopy (XPS) analysis revealed higher Cr concentration in the passive films of Fe0.5Cr steels, confirming the stabilization effect of chromium at the

oxide-metal interface. TEM analysis confirmed that amorphous Cr-containing oxide layers acted as an effective diffusion barrier against corrosive species, reducing the FAC rate [74].

Recent investigations have further confirmed the synergistic role of Cr, Mo, and Cu in enhancing FAC resistance by altering oxide composition, structure, and electrochemical stability. A 2023 study revealed that increasing Cr and Mo content in low-alloy steels significantly improved the uniformity and density of the oxide layer, reducing its solubility under high-velocity flow conditions [23]. In particular, Mo was found to integrate into the oxide matrix, forming stable Fe-Mo spinel structures that resist dissolution. Another study emphasized that Cu addition enhanced the protectiveness of the oxide layer, reducing the electron transfer rate at the metal-solution interface [147]. Advanced surface analysis showed that Mo- and Cu-enriched steels developed duplex oxide films—an inner compact magnetite layer and an outer amorphous mixed-metal oxide—offering superior corrosion protection in both deaerated and oxygenated water environments [148]. These findings are consistent with prior work demonstrating that multi-element alloying reduces the porosity of oxide layer and improves its adhesion to the substrate, both of which are critical to withstanding high-velocity coolant flow and minimizing FAC damage [149].

The integration of advanced characterization techniques provides robust evidence that, Crrich oxides significantly enhance corrosion resistance by stabilizing the oxide structure, densifying the rust layer, and reducing oxide dissolution rates [148]. Thus, optimizing Cr content is vital for improving the service life of pipelines against FAC.

6.2 Corrosion inhibitors

In NPPs, corrosion inhibitors are integral to maintaining the integrity of cooling systems and preventing material degradation under high-temperature and high-pressure conditions [150]. A diverse array of inhibitors has been employed to mitigate corrosion across different systems. For instance, film-forming amines (FFAs) [151], such as octadecylamine (ODA) [152] and oleyl propylenediamine (OLDA) [153], are utilized to create protective hydrophobic layers on metal surfaces, effectively reducing corrosion in water/steam circuits composed primarily of carbon steel. FFAs are particularly beneficial during various operational states, including startups, shutdowns, and maintenance periods. Inorganic inhibitors such as sodium molybdate [154], sodium nitrite [155], and sodium phosphate [156] have been formulated into compound inhibitors for cooling water systems in NPPs. These compounds work synergistically to maintain an alkaline environment, thereby minimizing corrosion rates in closed-loop systems. Additionally, polyethylenimine, polyvinylpyrrolidone, and 2-

mercaptobenzimidazole have been applied to prevent corrosion of mild steel in acidic media, showcasing the versatility of organic inhibitors in various chemical environments [157]. Figure 18 illustrates both the morphological impact of increasing inhibitor concentrations and a conceptual model of inhibitor behavior under high-velocity flow in contraction and expansion pipe zones. The selection of appropriate corrosion inhibitors is critical and depends on specific operational conditions, materials involved, and environmental considerations. Ongoing research and development continue to enhance the efficacy and environmental compatibility of these inhibitors, ensuring the prolonged safety and efficiency of NPP operations [150].

6.3 Maintenance strategies

Effective maintenance planning is essential for ensuring the continuous operation and safety of NPPs, particularly in managing degradation mechanisms of FAC. This is especially critical in Canada Deuterium Uranium (CANDU) reactors, where the feeder piping system—composed of hundreds of carbon steel inlet and outlet pipes—is highly susceptible to FAC-induced wall thinning and leakage, especially at outlet pipe bends [158], [159]. Since leakage in these systems can result in unplanned shutdowns and significant operational losses, the implementation of rigorous inspection and maintenance (I&M) strategies is a central component of FAC management programs.

Current I&M practices, adopted following the FAC-related incident at the Surry NPP in 1986, are governed by established guidelines that require regular inspections, accurate wall thickness measurements, predictive assessments of degradation trends, and the replacement of pipes that fall below a minimum wall thickness threshold [160]. These guidelines also emphasize the need to prioritize pipes previously uninspected or previously identified as near critical.

However, traditional rule-based approaches often lack optimization in terms of cost and reliability. They typically do not quantify system-level reliability targets, nor do they optimize maintenance efforts accordingly. To address these gaps, reliability-based inspection and maintenance (RBIM) frameworks have been developed. These frameworks integrate probabilistic deterioration models (such as Gamma processes) with Bayesian updating to incorporate real-time inspection data, allowing dynamic assessments of component reliability at both the individual and system levels [161], [162]. Such approaches enable more cost-effective and risk-informed maintenance scheduling.

RBIM strategies rely on heuristic optimization techniques to identify optimal inspection and repair plans based on system-wide reliability constraints. This framework can effectively

handle hidden failures, those only detectable through inspection—and large-scale systems with many deteriorating components, such as nuclear piping networks. While individual components are evaluated for inspection and maintenance needs, the system-level reliability target ensures a holistic approach that aligns maintenance frequency and timing with operational safety and cost-efficiency goals [163], [164], [165].

In summary, transitioning from rule-based to reliability-based maintenance strategies presents a significant opportunity for improving the economic and operational performance of FAC management in NPPs. This shift ensures better resource allocation, reduces unplanned outages, and extends component lifespans through targeted, data-informed interventions.

Although advances in alloy design, inhibitor chemistry and reliability-based maintenance have improved FAC control, important gaps persist. Alloy optimization (Cr, Mo, Cu) requires standardized threshold values and long-term validation under irradiated reactor environments [53], [74], [138], [149]. Inhibitors such as FFAs and inorganic salts look promising, but their effectiveness under high shear, multiphase flow, and radiation remains unknown. RBIM frameworks [161], [165] also need accurate degradation models that work with CFD/ML predictions and in-situ diagnostics to be reliable for making predictions. Filling these gaps will make it possible for next-generation NPPs to manage FAC in real time.

7. Future perspectives and research directions

Despite significant progress in understanding FAC in NPPs, important gaps remain that limit accurate prediction, long-term monitoring, and effective management. Traditional electrochemical and mass transfer models [38], [36], [35], [40], [41], [42], [44]. Oversimplify real reactor environments, where FAC is influenced by complex interactions among fluctuating water chemistry, radiation exposure, and localized flow geometries [3], [166], [167]. These models also neglect microstructural degradation mechanisms such as chromium depletion and grain boundary evolution [75], [168], and tend to treat synergistic effects like erosion, FAC, and irradiation in isolation [3], [169]. Figure 19 provides a visual summary of six key research directions: predictive models, diagnostics and real-time monitoring, materials and self-healing coatings, advanced testing systems, maintenance frameworks, and unresolved research gaps that collectively define the future perspectives for FAC mitigation

Moreover, non-destructive evaluation (NDE) techniques, including ultrasonic and infrared thermography methods [170], [171], although effective in wall-thickness assessment, face limitations in detecting localized early-stage corrosion. To overcome these limitations, future research must integrate environmental aging, site-specific turbulence, and irradiation effects

into more refined predictive models [62], [172]. Advanced diagnostics—such as synchrotron-based X-ray imaging, atom probe tomography (APT), and in situ electron microscopy—are also needed to gain detailed insight into oxide degradation and localized corrosion kinetics. The development of resilient materials with self-healing oxide layers and real-time monitoring-informed, adaptive maintenance strategies will be essential for ensuring the long-term safety and performance of next-generation nuclear reactors [173], [174].

721

722

723

724

725

726

727

728

729

730

731

732

733

734

735

736

737

738

739

740

741

742

743

744

745

746

747

748

749

750

751

752

753

754

Despite progress, one of the future plans is to combine real-time monitoring and self-healing materials to combat FAC in nuclear systems. The monitoring technique could be based on networks of embedded sensors (electrochemical probes, fiber-optic or ultrasonic devices) that provide the in situ monitoring of the wall thinning and corrosion rates and thus promptly identify FAC hotspots and intervene [175], [176]. This represents a transition away within periodic inspection to a continuous online health monitoring platform - e.g., wireless corrosion sensor platforms are being designed to operate in harsh environments (such as nuclear reactors) to provide distributed real-time wall-thickness information without involving direct human access [177]. With this kind of high-resolution monitoring, adaptive maintenance is possible: when sensors detect abnormal thinning, repairs or flow chemistry changes can be initiated, rather than waiting for scheduled outages. Self-healing materials and intelligent coatings provide proactive protection by automatically repairing or mitigating corrosion damage. Advanced anti-FAC coatings are being developed with microcapsules or nanocontainers built into the coating and containing corrosion inhibitors or polymerisable agents that are released during coating damage [178]. These bio-inspired coatings mimic an "immune response," detecting microscopic damage and triggering chemical healing reactions that halt FAC at its inception [178]. In parallel, next-generation reactor developmental alloys place a premium on self-passivating oxides with great resilience. For instance, high-chromium steels or Ni-based alloys (e.,g. Inconel) can develop stable chromium oxide layers that readily re-passivate rapidly after breakdown, acting as self-healing oxide layers against FAC attack. Maintaining such protective oxide scales is especially crucial in advanced reactor coolants (e.,g. liquid leadbismuth) where a robust, regenerative oxide layer prevents accelerated corrosion of steel components [179]. By combining continuous sensor feedback with materials that can heal or re-protect themselves in service, future FAC management will shift toward predictive and selfadaptive approaches, enhancing the safety and longevity of critical reactor components

While current research identifies environmental conditions, hydrodynamics, and material properties as key factors influencing FAC [49], [50], [51], important limitations persist. Environmental models often neglect transient chemistry, radiolysis effects, and operational

variability [3], [166], [167]. Hydrodynamic studies frequently rely on simplified geometries, overlooking the effects of fluid-structure interactions present in actual systems [14], [180], [65]. Alloy development has made strides [35], [66], [67], [68], but long-term aging and radiation-assisted degradation in steels remain underexplored [70], [71], [72], [73]. Recent diagnostic advances, including PIV, CFD-LES, and nanoscale characterization [59], [60], [61], [62], [170], [171], offer new opportunities, but require wider integration into real-time monitoring. Future models must incorporate localized flow, radiation effects, and evolving surface conditions into unified, multi-physics platforms to support safer and more durable reactor designs [173], [174].

Although current corrosion testing methods such as, vibration diagnostics [109],[110], stirred autoclaves [113], [114], and advanced systems like RCE/RDE and jet impingement autoclaves [122], [123], [128], [129], have improved our understanding toward FAC mechanism, these corrosion testing methods fall short of replicating real reactor conditions. Vibration-based techniques show diagnostic potential but require ML and advanced signal processing for improved accuracy under in-service conditions [110], [111], [112]. Stirred autoclaves simulate chemical environments well but not high-shear turbulence, prompting the adoption of systems like rotating cage autoclaves [135], [136]. While these provide better flow realism, their complexity and lack of multi-parameter in situ monitoring limit practical deployment. Future testing should integrate high-fidelity flow simulations, real-time electrochemical diagnostics, and artificial intelligence (AI)-driven analysis to enhance FAC prediction and mitigation in nuclear environments.

Classical models like Sánchez-Caldera [88], [89], [90] and CEGB [181], [182] provide foundational insight into FAC, but these models are limited by their applicability to simplified flow conditions and outdated datasets. Even newer models, such as Ducreux [97] that include material-specific factors, lack spatial resolution. CFD-based models [99], [100], [183], [101] offer detailed flow simulations. These models, however, also face challenges in validation, surface roughness modeling, and corrosion kinetics integration. ML approaches [106], [107] improve predictive accuracy by capturing complex variable interactions but currently lack interpretability and regulatory readiness. Future models should combine physical and data-driven techniques, prioritize experimental validation, and align with situ monitoring to support adaptive, real-time FAC management.

FAC mitigation relies on three key strategies: alloy optimization, corrosion inhibitors, and maintenance planning. Cr-, Mo-, and Cu-enriched steels improve corrosion resistance, but long-term validation under reactor conditions is still required [23], [53], [129], [78], [79], [80].

Inhibitors like film-forming amines and inorganic compounds remain vital, though their performance under multiphase flow and irradiation requires further research [150], [151], [152], [153]. Traditional rule-based maintenance is being replaced by reliability-based frameworks (RBIM), offering more efficient, data-driven planning [158], [159], [160]. Future FAC control should integrate advanced materials, adaptive inhibitors, and AI-enhanced maintenance for predictive, real-time protection.

795

796

797

798

799

800

801

802

803

804

805

806

807

808

809

810

811

812

813

814

815

816

817

789

790

791

792

793

794

Conclusion

FAC remains a dominant threat to the structural reliability and longevity of NPP components. This paper comprehensively reviews various mechanisms of FAC, models used to predict FAC rate of metals, and potential mitigation strategies. Corrosion testing techniques and factors influencing FAC rate were also discussed. Despite advances in understanding electrochemical and hydrodynamic foundations of FAC, current predictive models and experimental tools often fall short of fully capturing the complex, real-world conditions in NPP environments. While significant progress has been made in alloy development and the application of corrosion inhibitors, their long-term performance under multiphase flow and irradiation still requires further investigation. Non-destructive evaluation methods and testing platforms need to evolve toward more realistic, high-shear, and turbulent flow simulations. The integration of CFD, ML, and advanced diagnostic techniques holds promise for improving predictive accuracy and maintenance planning. The future of FAC mitigation in nuclear systems lies in the convergence of real-time monitoring, smart material design, and data-driven maintenance strategies. A robust, multi-disciplinary research effort is essential to transition from reactive management to predictive, condition-based operation, ensuring the continued safety and efficiency of nuclear energy infrastructure.

Acknowledgements

The authors acknowledge the support provided by Interdisciplinary Research Center for Industrial Nuclear Energy (IRC-INE) at King Fahd University of Petroleum and Minerals (KFUPM), Dhahran, Saudi Arabia, under the research grant# INNE2405 for conducting this research work.

818 **Author Contributions** 819 M.A.AbedAllah, Muhammad Arroussi and O.K.Siddiqui wrote the article. M. Yusaf and TN 820 Hunter revised the draft with his input. IH Toor provided the manuscript concept and reviewed 821 the final draft. A.Shams acquired the funding and reviewed the article. 822 **Competing Interests** 823 The authors declare no competing interests. 824 Data availability 825 Not applicable. 826 References 827 K. Grandin, P. Jagers, S. Kullander, Nuclear Energy, Ambio 39 (2010) 26–30. [1] 828 https://doi.org/10.1007/s13280-010-0061-0. 829 [2] B.N. Hanna, A. Abou-Jaoude, N. Guaita, P. Talbot, C. Lohse, Navigating 830 Economies of Scale and Multiples for Nuclear-Powered Data Centers and Other 831 Applications with High Service Availability Needs, Energies (Basel) 17 (2024) 832 5073. https://doi.org/10.3390/en17205073. 833 J. Krūmiņš, M. Kļaviņš, Investigating the Potential of Nuclear Energy in Achieving a [3] 834 Carbon-Free Energy Future, Energies (Basel) 16 (2023) 3612. https://doi.org/10.3390/en16093612. 835 836 [4] E.K. Addo, A.T. Kabo-bah, F.A. Diawuo, S.K. Debrah, The Role of Nuclear Energy in 837 Reducing Greenhouse Gas (GHG) Emissions and Energy Security: A Systematic 838 Review, Int J Energy Res 2023 (2023) 1–31. https://doi.org/10.1155/2023/8823507. 839 V. Kain, S. Roychowdhury, P. Ahmedabadi, D.K. Barua, Flow accelerated [5] 840 corrosion: Experience from examination of components from nuclear power 841 plants, Eng Fail Anal 18 (2011) 2028-2041. https://doi.org/10.1016/j.engfailanal.2011.06.007. 842 843 S.J. Zinkle, G.S. Was, Materials challenges in nuclear energy, Acta Mater 61 (2013) [6] 844 735–758. https://doi.org/10.1016/j.actamat.2012.11.004. 845 [7] O.S.I. Fayomi, I.G. Akande, S. Odigie, Economic Impact of Corrosion in Oil Sectors 846 and Prevention: An Overview, J Phys Conf Ser 1378 (2019) 022037.

https://doi.org/10.1088/1742-6596/1378/2/022037.

- T. Bai, P. Chen, K. Guan, Evaluation of stress corrosion cracking susceptibility of stainless steel 304L with surface nanocrystallization by small punch test, Mater Sci Eng A 561 (2013) 498–506. https://doi.org/10.1016/j.msea.2012.10.071.
- M. Arroussi, J. Wu, L. Zhu, P. Wang, D. Zhang, W. Wang, Effect of preferential growth of Shewanella oneidensis MR-1 on microbial corrosion of constituent phases of 2205 duplex stainless steel, Bioelectrochemistry 163 (2025) 108859. https://doi.org/10.1016/j.bioelechem.2024.108859.
- [10] S.-S. Kang, S.-S. Hwang, H.-P. Kim, Y.-S. Lim, J.-S. Kim, The experience and
 analysis of vent pipe PWSCC (primary water stress corrosion cracking) in PWR
 vessel head penetration, Nucl Eng Des 269 (2014) 291–298.
 https://doi.org/10.1016/j.nucengdes.2013.08.043.
- Z. Liu, J. Wang, Z. Qin, D.-H. Xia, Y. Behnamian, W. Hu, B. Tribollet, A mechanistic study on stress corrosion cracking of sensitized AA5083 in a simulated water level fluctuation zone: Combined impedance analysis and tensile tests, Corros Sci 245 (2025) 112701. https://doi.org/10.1016/j.corsci.2025.112701.
- [12] G.S. Was, C.-B. Bahn, J. Busby, B. Cui, D. Farkas, M. Gussev, M. Rigen He, J.
 Hesterberg, Z. Jiao, D. Johnson, W. Kuang, M. McMurtrey, I. Robertson, A. Sinjlawi,
 M. Song, K. Stephenson, K. Sun, S. Swaminathan, M. Wang, E. West, How
 irradiation promotes intergranular stress corrosion crack initiation, Prog Mater Sci
 143 (2024) 101255. https://doi.org/10.1016/j.pmatsci.2024.101255.
- 868 [13] B. Jiang, X. Du, Q. Peng, B. Zhang, Y. Chen, Z. Jiao, Y. He, Y. Pan, W. Yang, Y. Deng,
 869 L. Qiao, The impact of alloying elements on the irradiation and hydrogen-induced
 870 corrosion of the austenite in nuclear stainless steel, Corros Sci 249 (2025)
 871 112859. https://doi.org/10.1016/j.corsci.2025.112859.
- P. Madasamy, P. Chandramohan, M. Mukunthan, T.V. Krishna Mohan, S.
 Rangarajan, N. Uttam, R. Ramakrishnan, G. Babulal, H.P. Rani, P. Surendran, A.K.
 Gupta, J.P. Nair, Flow accelerated corrosion rate on carbon steel pipe bend by thin
 layer activation technique and computational modeling: Under PHWR operating
 conditions, Eng Fail Anal 121 (2021) 105125.
 https://doi.org/10.1016/j.engfailanal.2020.105125.
- Wael H. Ahmed, Flow Accelerated Corrosion in Nuclear Power Plants, in: Nuclear Power-Practical Aspects, InTech, 2012. https://doi.org/10.5772/51346.
- K. Fujiwara, M. Domae, K. Yoneda, F. Inada, Model of physico-chemical effect on
 flow accelerated corrosion in power plant, Corros Sci 53 (2011) 3526–3533.
 https://doi.org/10.1016/j.corsci.2011.06.027.
- 883 [17] W.H. Ahmed, M.M. Bello, M. El Nakla, A. Al Sarkhi, H.M. Badr, Experimental investigation of flow accelerated corrosion under two-phase flow conditions,

885 886		Nucl Eng Des 267 (2014) 34–43. https://doi.org/10.1016/j.nucengdes.2013.11.073.
887 888 889 890	[18]	SB. Oh, J. Kim, JY. Lee, DJ. Kim, KM. Kim, Analysis of pipe thickness reduction according to pH in FAC facility with In situ ultrasonic measurement real time monitoring, Nucl Eng Technol 54 (2022) 186–192. https://doi.org/10.1016/j.net.2021.07.048.
891 892 893	[19]	T. Le, D. Ewing, C. Schefski, C.Y. Ching, Mass transfer in back-to-back elbows arranged in an out of plane configuration, Nucl Eng Des 270 (2014) 209–216. https://doi.org/10.1016/j.nucengdes.2014.01.004.
894 895 896 897	[20]	J.C. Fornaciari, LC. Weng, S.M. Alia, C. Zhan, T.A. Pham, A.T. Bell, T. Ogitsu, N. Danilovic, A.Z. Weber, Mechanistic understanding of pH effects on the oxygen evolution reaction, Electrochim Acta 405 (2022) 139810. https://doi.org/10.1016/j.electacta.2021.139810.
898 899 900 901 902 903	[21]	O. de Bouvier, M. Bouchacourt, K. Fruzzetti, Redox conditions effect on flow accelerated corrosion: Influence of hydrazine and oxygen, in: International Conference on Water Chemistry in Nuclear Reactor Systems – Operation Optimisation and New Developments (Chemistry 2002), International Atomic Energy Agency (IAEA) / Société Française d'Énergie Nucléaire (SFEN), Avignon, France, 2002: p. 10.
904 905 906	[22]	T. Satoh, Y. Shao, W.G. Cook, D.H. Lister, S. Uchida, Flow-Assisted Corrosion of Carbon Steel Under Neutral Water Conditions, Corrosion 63 (2007) 770–780. https://doi.org/10.5006/1.3278426.
907 908 909 910	[23]	S. Kim, G. Kim, SW. Song, J.H. Kim, Effects of Cr and Mo contents on the flow-accelerated corrosion behavior of low alloy steels in the secondary side of pressurized water reactors, J Nucl Mater 585 (2023) 154652. https://doi.org/10.1016/j.jnucmat.2023.154652.
911 912 913 914	[24]	DJ. Kim, SW. Kim, J.Y. Lee, K.M. Kim, S.B. Oh, G.G. Lee, J. Kim, SS. Hwang, M.J. Choi, Y.S. Lim, S.H. Cho, H.P. Kim, Flow-accelerated corrosion assessment for SA106 and SA335 pipes with elbows and welds, Nucl Eng Technol 53 (2021) 3003-3011. https://doi.org/10.1016/j.net.2021.03.026.
915 916 917 918	[25]	H. Yun, SJ. Moon, YJ. Oh, Development of wall-thinning evaluation procedure for nuclear power plant piping - Part 2: Local wall-thinning estimation method, Nucl Eng Technol 52 (2020) 2119–2129. https://doi.org/10.1016/j.net.2020.03.001.
919 920 921	[26]	D. Rao, B. Kuang, X. Zhang, S. Zhang, Study of CAP1400 secondary pipe wall thinning rate under flow accelerated corrosion, Ann Nucl Energy 155 (2021) 108170. https://doi.org/10.1016/j.anucene.2021.108170.

922 923 924	[27]	L. Zeng, G.A. Zhang, X.P. Guo, C.W. Chai, Inhibition effect of thioureidoimidazoline inhibitor for the flow accelerated corrosion of an elbow, Corros Sci 90 (2015) 202–215. https://doi.org/10.1016/j.corsci.2014.10.011.
925 926 927	[28]	N. Katagiri, A. Kioka, M. Nonoyama, Y. Hayashi, Inhibiting flow-accelerated copper corrosion under liquid jet impingement by utilizing nanobubbles, Surfaces and Interfaces 40 (2023) 103067. https://doi.org/10.1016/j.surfin.2023.103067.
928 929 930	[29]	Kazutoshi Fujiwara, Kimitoshi Yoneda, Fumio Inada, Effect of Dissolved Oxygen on Flow-Accelerated Corrosion in Neutral and Alkaline Solutions, N European Federation of Corrosion (EFC) Publications (n.d.) 1–10.
931 932 933	[30]	K. Fujiwara, K. Yoneda, Effects of Ph and Cr Content of Materials on Flow-Accelerated Corrosion and Their Prediction, (2023). https://doi.org/10.2139/ssrn.4529423.
934 935 936 937	[31]	P. Madasamy, T.V. Krishna Mohan, A. Sylvanus, E. Natarajan, H.P. Rani, S. Velmurugan, Hydrodynamic effects on flow accelerated corrosion at 120 °C and neutral pH conditions, Eng Fail Anal 94 (2018) 458–468. https://doi.org/10.1016/j.engfailanal.2018.08.021.
938 939 940 941	[32]	S. KM, B.M. Praveen, B.K. Devendra, A review on corrosion inhibitors: Types, mechanisms, electrochemical analysis, corrosion rate and efficiency of corrosion inhibitors on mild steel in an acidic environment, Results in Surfaces and Interfaces 16 (2024) 100258. https://doi.org/10.1016/j.rsurfi.2024.100258.
942 943 944 945	[33]	S. Järvimäki, T. Saario, K. Sipilä, M. Bojinov, Effect of hydrazine on general corrosion of carbon and low-alloyed steels in pressurized water reactor secondary side water, Nucl Eng Des 295 (2015) 106–115. https://doi.org/10.1016/j.nucengdes.2015.08.033.
946 947 948	[34]	E. Gipon, S. Trevin, Flow-accelerated corrosion in nuclear power plants, in: Nuclear Corrosion, Elsevier, 2020: pp. 213–250. https://doi.org/10.1016/B978-0-12-823719-9.00006-8.
949 950 951	[35]	P. Khunphakdee, B. Chalermsinsuwan, Review of flow accelerated corrosion mechanism, numerical analysis, and control measures, Chem Eng Res Des 197 (2023) 519–535. https://doi.org/10.1016/j.cherd.2023.08.012.
952 953	[36]	V. Kain, Flow Accelerated Corrosion: Forms, Mechanisms and Case Studies, Procedia Eng 86 (2014) 576–588. https://doi.org/10.1016/j.proeng.2014.11.083.
954 955	[37]	SI. Seo, A Two-phase FAC Study on Heat Recovery Steam Generator, J Power Syst Eng 26 (2022) 64–71. https://doi.org/10.9726/kspse.2022.26.5.064.
956 957	[38]	T.S. Ajmal, S.B. Arya, K.R. Udupa, Effect of hydrodynamics on the flow accelerated corrosion (FAC) and electrochemical impedance behavior of line

958 pipe steel for petroleum industry, International Journal of Pressure Vessels and 959 Piping 174 (2019) 42–53. https://doi.org/10.1016/j.ijpvp.2019.05.013. 960 [39] Y. Hu, Y.H. Lu, L. Xin, Y.M. Han, C. Hong, Effect of microstructure and bending 961 angle in cold bend pipe of SA 106B on flow accelerated corrosion behavior in 962 simulated pressurized water reactor secondary circuit water environment, Corros 963 Sci 232 (2024) 112017. https://doi.org/10.1016/j.corsci.2024.112017. 964 [40] T. Xu, R. Zhang, X. Si, Effects of fluid dynamics parameters on flow-accelerated 965 corrosion at elbow of carbon steel pipeline, Mater Res Express 11 (2024) 056520. 966 https://doi.org/10.1088/2053-1591/ad4c3c. 967 M. Qin, S. Chen, N. Ye, Y. Chen, S. Zhang, K. Li, K. Liao, Study on the evolution [41] 968 mechanism and influencing factors of CO2 corrosion product film under pipe 969 flow, International Journal of Pressure Vessels and Piping 216 (2025) 105506. 970 https://doi.org/10.1016/j.ijpvp.2025.105506. 971 [42] S. Moon, J.-Y. Lee, K.-M. Kim, S.-W. Han, G.-G. Lee, W.-Y. Maeng, D.-J. Kim, H. Jo, 972 S.H. Kim, Hydrodynamic parameters affecting flow-accelerated corrosion in 973 elbows, Nucl Eng Technol 57 (2025) 103293. 974 https://doi.org/10.1016/j.net.2024.10.055. 975 [43] G. Yamazaki, K. Fujiwara, Flow, chloride, and pH effects on carbon steel corrosion 976 in BWR cold shutdown: Development of a 4-STEP corrosion model, Corros Sci 977 253 (2025) 112960. https://doi.org/10.1016/j.corsci.2025.112960. 978 H. Okada, S. Uchida, M. Naitoh, J. Xiong, S. Koshizuka, Evaluation Methods for [44] 979 Corrosion Damage of Components in Cooling Systems of Nuclear Power Plants 980 by Coupling Analysis of Corrosion and Flow Dynamics (V) Flow-Accelerated 981 Corrosion under Single- and Two-phase Flow Conditions, J Nucl Sci Technol 48 982 (2011) 65-75. https://doi.org/10.1080/18811248.2011.9711680. 983 L. Yang, D. Zhang, H. Fan, X. Fu, R. Yan, Z. Wei, H. Wu, In-situ electrochemical [45] 984 testing and fluid dynamics simulation of pipeline defects under flow accelerated 985 corrosion, Exp Therm Fluid Sci 150 (2024) 111048. https://doi.org/10.1016/j.expthermflusci.2023.111048. 986 987 S. Uchida, M. Naitoh, H. Okada, Y. Uehara, S. Koshizuka, Evaluation of flow [46] 988 accelerated corrosion by coupled analysis of corrosion and flow dynamics. 989 Relationship of oxide film thickness, hematite/magnetite ratio, ECP and wall 990 thinning rate, Nucl Eng Des 241 (2011) 4585-4593. 991 https://doi.org/10.1016/j.nucengdes.2010.09.018. 992 T. Ma, D. Li, L. Zeng, H. Chen, Comparative investigation on high-pressure flow 993 accelerated corrosion at gradual contraction and gradual expansion pipes,

Corros Sci 228 (2024) 111803. https://doi.org/10.1016/j.corsci.2023.111803.

995 K. Ishida, Y. Wada, T. Shimaoka, R. Shimizu, Flow accelerated corrosion of carbon [48] 996 steel containing chromium under water chemistry conditions of boiling water 997 reactor applying mitigation techniques of corrosive environment, J Nucl Sci 998 Technol 59 (2022) 709-724. https://doi.org/10.1080/00223131.2021.2004951. 999 R. Galván-Martínez, C. Campechano-Lira, R. Orozco-Cruz, M.Á. Hernández-[49] 1000 Pérez, F. López-Huerta, E. Mejía-Sánchez, J.A. Ramírez-Cano, A. Carmona-1001 Hernández, Effect of Hydrodynamic Conditions on the Corrosion Mechanism of 1002 HSLA X100 Steel by EIS and EN Analysis, Surfaces 8 (2025) 10. 1003 https://doi.org/10.3390/surfaces8010010. 1004 [50] Y. Xu, Q. Zhang, Q. Zhou, S. Gao, B. Wang, X. Wang, Y. Huang, Flow accelerated 1005 corrosion and erosion-corrosion behavior of marine carbon steel in natural 1006 seawater, Npj Mater Degrad 5 (2021) 56. https://doi.org/10.1038/s41529-021-1007 00205-1. 1008 [51] G. Liu, B. Liang, Z. Ding, Effect of oxidation temperature on surface oxide film 1009 structure and corrosion resistance of 50 steel, Heliyon 10 (2024) e40499. 1010 https://doi.org/10.1016/j.heliyon.2024.e40499. 1011 H. Zeng, Y. Yang, M. Zeng, M. Li, Effect of dissolved oxygen on electrochemical [52] 1012 corrosion behavior of 2205 duplex stainless steel in hot concentrated seawater, J 1013 Mater Sci Technol 66 (2021) 177–185. https://doi.org/10.1016/j.jmst.2020.06.030. 1014 [53] R.B. Dooley, V.K. Chexal, Flow-accelerated corrosion of pressure vessels in fossil 1015 plants, International Journal of Pressure Vessels and Piping 77 (2000) 85–90. https://doi.org/10.1016/S0308-0161(99)00087-3. 1016 1017 [54] Y. Dai, X. Zheng, P. Ding, Review on sodium corrosion evolution of nuclear-grade 1018 316 stainless steel for sodium-cooled fast reactor applications, Nucl Eng Technol 1019 53 (2021) 3474–3490. https://doi.org/10.1016/j.net.2021.05.021. 1020 Y. Utanohara, M. Murase, Influence of flow velocity and temperature on flow [55] 1021 accelerated corrosion rate at an elbow pipe, Nucl Eng Des 342 (2019) 20-28. 1022 https://doi.org/10.1016/j.nucengdes.2018.11.022. 1023 [56] V. Kain, S. Roychowdhury, T. Mathew, A. Bhandakkar, Flow accelerated corrosion 1024 and its control measures for the secondary circuit pipelines in Indian nuclear 1025 power plants, J Nucl Mater 383 (2008) 86-91. 1026 https://doi.org/10.1016/j.jnucmat.2008.08.024. 1027 Y. Utanohara, Y. Nagaya, A. Nakamura, M. Murase, K. Kamahori, Correlation [57] 1028 between Flow Accelerated Corrosion and Wall Shear Stress Downstream from an 1029 Orifice, Journal of Power and Energy Systems 7 (2013) 138–147. 1030 https://doi.org/10.1299/jpes.7.138.

1031 [58] W.H. Ahmed, M.M. Bello, M. El Nakla, A. Al Sarkhi, Flow and mass transfer 1032 downstream of an orifice under flow accelerated corrosion conditions, Nucl Eng 1033 Des 252 (2012) 52–67. https://doi.org/10.1016/j.nucengdes.2012.06.033. 1034 V. Harrandt, Y. Bazaikin, F. Huchet, J. Tihon, J. Havlica, Theory for [59] 1035 electrodiffusional wall shear stress measurement by directionally sensitive twin 1036 semicircular probe, Int J Heat Mass Transf 235 (2024) 126191. 1037 https://doi.org/10.1016/j.ijheatmasstransfer.2024.126191. 1038 [60] F. Shan, S.Y. Qin, Y. Xiao, A. Watanabe, M. Kano, F.Y. Zhou, Z.C. Liu, W. Liu, Y. Tsuji, 1039 Large-scale energetic coherent structures and their effects on wall mass transfer 1040 rate behind orifice in round pipe, J Fluid Mech 927 (2021) A8. 1041 https://doi.org/10.1017/jfm.2021.761. 1042 S. Moon, J.Y. Lee, K.-M. Kim, S.-W. Han, G.-G. Lee, W.-Y. Maeng, S. Oh, D.-J. Kim, [61] 1043 Assessment of flow-accelerated corrosion-induced wall thinning in SA106 pipes 1044 with elbow sections, Nucl Eng Technol (2023). 1045 https://doi.org/10.1016/j.net.2023.11.027. 1046 H.P. Rani, T. Divya, R.R. Sahaya, V. Kain, D.K. Barua, CFD study of flow [62] 1047 accelerated corrosion in 3D elbows, Ann Nucl Energy 69 (2014) 344–351. 1048 https://doi.org/10.1016/j.anucene.2014.01.031. 1049 G.A. Zhang, L. Zeng, H.L. Huang, X.P. Guo, A study of flow accelerated corrosion [63] 1050 at elbow of carbon steel pipeline by array electrode and computational fluid 1051 dynamics simulation, Corros Sci 77 (2013) 334-341. https://doi.org/10.1016/j.corsci.2013.08.022. 1052 1053 R. Vortmeyer-Kley, U. Gräwe, U. Feudel, Detecting and tracking eddies in oceanic [64] 1054 flow fields: a Lagrangian descriptor based on the modulus of vorticity, Nonlinear 1055 Process Geophys 23 (2016) 159–173. https://doi.org/10.5194/npg-23-159-2016. 1056 D.G. Kang, M.J. Jhung, S.H. Chang, Fluid-structure interaction analysis for [65] 1057 pressurizer surge line subjected to thermal stratification, Nucl Eng Des 241 (2011) 1058 257–269. https://doi.org/10.1016/j.nucengdes.2010.10.023. 1059 [66] G. Zheng, B. Kelleher, G. Cao, M. Anderson, T. Allen, K. Sridharan, Corrosion of 1060 316 stainless steel in high temperature molten Li2BeF4 (FLiBe) salt, J Nucl Mater 1061 461 (2015) 143-150. https://doi.org/10.1016/j.jnucmat.2015.03.004. 1062 [67] D.H. Zhang, X.C. Meng, G.Z. Zuo, M. Huang, L. Li, W. Xu, C.L. Li, Z.L. Tang, J.S. 1063 Yuan, Y.B. Liu, X.G. Cao, J.S. Hu, Study of the corrosion characteristics of 304 and 1064 316L stainless steel in the static liquid lithium, J Nucl Mater 553 (2021) 153032.

https://doi.org/10.1016/j.jnucmat.2021.153032.

1066 [68] G. Zheng, K. Sridharan, Corrosion of Structural Alloys in High-Temperature Molten 1067 Fluoride Salts for Applications in Molten Salt Reactors, JOM 70 (2018) 1535-1541. 1068 https://doi.org/10.1007/s11837-018-2981-2. 1069 B. Wang, Y. Wang, Q. Li, H. Li, L. Zhang, M. Lu, Effect of chromium on the [69] 1070 corrosion behaviour of low Cr-bearing alloy steel under an extremely high flow 1071 rate, RSC Adv 10 (2020) 35302-35309. https://doi.org/10.1039/D0RA04334F. 1072 [70] B. Fournier, F. Dalle, M. Sauzay, J. Longour, M. Salvi, C. Caës, I. Tournié, P.-F. 1073 Giroux, S.-H. Kim, Comparison of various 9–12%Cr steels under fatigue and 1074 creep-fatigue loadings at high temperature, Mater Sci Eng A 528 (2011) 6934-1075 6945. https://doi.org/10.1016/j.msea.2011.05.046. 1076 [71] S. Kim, T. Kim, Y. Lee, J.H. Kim, Soft X-ray study on electronic structure of passive 1077 oxide layer of carbon steel and low alloy steel in flow-accelerated corrosion 1078 environments of pressurized water reactors, Corros Sci 159 (2019) 108143. 1079 https://doi.org/10.1016/j.corsci.2019.108143. 1080 [72] R.L. Klueh, Elevated temperature ferritic and martensitic steels and their 1081 application to future nuclear reactors, International Materials Reviews 50 (2005) 1082 287-310. https://doi.org/10.1179/174328005X41140. 1083 [73] R. Klueh, D. Harries, High-Chromium Ferritic and Martensitic Steels for Nuclear 1084 Applications, ASTM International, 100 Barr Harbor Drive, PO Box C700, West 1085 Conshohocken, PA 19428-2959, 2001. https://doi.org/10.1520/MONO3-EB. 1086 S. Jiang, F. Chai, H. Su, C. Yang, Influence of chromium on the flow-accelerated [74] 1087 corrosion behavior of low alloy steels in 3.5% NaCl solution, Corros Sci 123 1088 (2017) 217–227. https://doi.org/10.1016/j.corsci.2017.04.024. 1089 M. Sireesha, S.K. Albert, S. Sundaresan, Metallurgical changes and mechanical [75] 1090 behaviour during high temperature aging of welds between Alloy 800 and 316LN 1091 austenitic stainless steel, Materials Science and Technology 19 (2003) 1411-1092 1417. https://doi.org/10.1179/026708303225006042. 1093 M.B. Anoop, K. Balaji Rao, N. Lakshmanan, Safety assessment of austenitic steel [76] 1094 nuclear power plant pipelines against stress corrosion cracking in the presence of 1095 hybrid uncertainties, International Journal of Pressure Vessels and Piping 85 1096 (2008) 238-247. https://doi.org/10.1016/j.ijpvp.2007.09.001. 1097 [77] P. Bouin, A. Fissolo, C. Gourdin, Study of the Crack Propagation Behaviour of 304L 1098 Austenitic Stainless Steel Under Thermal Fatigue, in: Volume 3: Design and 1099 Analysis, ASMEDC, 2011: pp. 495-503. https://doi.org/10.1115/PVP2011-57234. 1100 [78] S. Bradaï, C. Gourdin, S. Courtin, J.C. Le Roux, C. Gardin, Equi-Biaxial Loading

Effect on Austenitic Stainless Steel Fatigue Life, in: Volume 3: Design and

1102 1103		Analysis, American Society of Mechanical Engineers, 2014. https://doi.org/10.1115/PVP2014-28421.
1104 1105 1106 1107	[79]	S. Kavithaa, S. George Shaji, V. Bhandiwad, Electron beam welding of oxide dispersion strengthened 9 Cr martensitic steel-an experimental and theoretical perspective, Mater Today Proc 22 (2020) 2509–2519. https://doi.org/10.1016/j.matpr.2020.03.379.
1108 1109 1110 1111	[80]	X. Schuler, KH. Herter, J. Rudolph, Derivation of Design Fatigue Curves for Austenitic Stainless Steel Grades 1.4541 and 1.4550 Within the German Nuclear Safety Standard KTA 3201.2, in: Volume 1B: Codes and Standards, American Society of Mechanical Engineers, 2013. https://doi.org/10.1115/PVP2013-97138.
1112 1113 1114 1115	[81]	F. Xue, F. Shi, C. Zhang, Q. Zheng, D. Yi, X. Li, Y. Li, The Microstructure and Mechanical and Corrosion Behaviors of Thermally Aged Z3CN20-09M Cast Stainless Steel for Primary Coolant Pipes of Nuclear Power Plants, Coatings 11 (2021) 870. https://doi.org/10.3390/coatings11080870.
1116 1117 1118 1119	[82]	M.E. Ibrahim, M. Marzbali, A.K. Gujba, M. Medraj, The role of hardening and roughening during the incubation period in water droplet impingement erosion of Ti–6Al–4V, Wear 520–521 (2023) 204658. https://doi.org/10.1016/j.wear.2023.204658.
1120 1121 1122	[83]	Y. Dai, X. Zheng, P. Ding, Review on sodium corrosion evolution of nuclear-grade 316 stainless steel for sodium-cooled fast reactor applications, Nucl Eng Technol 53 (2021) 3474–3490. https://doi.org/10.1016/j.net.2021.05.021.
1123 1124 1125	[84]	A. Saeed, Developed borated austenitic stainless steel alloys as nuclear reactor control rods, Nucl Eng Des 413 (2023) 112515. https://doi.org/10.1016/j.nucengdes.2023.112515.
1126 1127 1128 1129	[85]	S. Chen, H. Zhuang, J. Guo, Y. Li, W. Wang, Q. Guo, Unified analysis of the effect of mill scale on the passivation and corrosion of nuclear containment steel liner in simulated concrete pore solutions, Constr Build Mater 441 (2024) 137463. https://doi.org/10.1016/j.conbuildmat.2024.137463.
1130 1131 1132 1133	[86]	X. Li, J. Gong, Fragility and Leakage Risk Assessment of Nuclear Containment Structure under Loss-of-Coolant Accident Conditions Considering Liner Corrosion, Applied Sciences 14 (2024) 2407. https://doi.org/10.3390/app14062407.
1134 1135 1136 1137	[87]	J. Huang, D. Lister, S. Uchida, The corrosion of aluminum alloy and release of hydrogen in nuclear reactor emergency core coolant: Implications for deflagration and explosion risk, Nucl Eng Des 359 (2020) 110458. https://doi.org/10.1016/j.nucengdes.2019.110458.

1138 [88] L.E. Sanchez-Caldera, P. Griffith, E. Rabinowicz, The Mechanism of Corrosion-1139 Erosion in Steam Extraction Lines of Power Stations, J Eng Gas Turbine Power 110 1140 (1988) 180–184. https://doi.org/10.1115/1.3240099. 1141 [89] Mikko Vepsäläinen, Timo Saario, Magnetite dissolution and deposition in NPP 1142 secondary circuit, Espoo, Finland, 2010. 1143 [90] Iva Betova, Martin Bojinov, Timo Saario, Predictive modelling of flow-accelerated 1144 corrosion-unresolved problems and issues, Espoo, Finland, 2010. 1145 Ruixuan Han, Yi Peng, Huailin Li, Prediction Model for Oxidation Layer Thickness [91] 1146 in Flow Accelerated Corrosion, in: ASME 2014 22nd International Conference on 1147 Nuclear Engineering, ASME, Prague, Czech Republic, 2014. 1148 [92] S. Trevin, M. Persoz, T. Knook, FAC Calculations With BRT-CICERO™ and Updating to Version 3.0, in: ASME 2009 17th International Conference on Nuclear 1149 1150 Engineering, ASME, Brussels, Belgium, 2009: pp. 84-88. H. Subramanian, P. Madasamy, H. Kumawat, R.G. Thomas, T.V. Krishnamohan, S. 1151 [93] 1152 Velmurugan, S.V. Narasimhan, Thin layer activation for probing flow accelerated corrosion of carbon steel, Corros Sci 54 (2012) 45-51. 1153 https://doi.org/10.1016/j.corsci.2011.08.044. 1154 1155 [94] B. Poulson, Predicting and Preventing Flow Accelerated Corrosion in Nuclear Power Plant, International Journal of Nuclear Energy 2014 (2014) 1–23. 1156 1157 https://doi.org/10.1155/2014/423295. 1158 [95] G.D. Song, S.-H. Jeon, Y.-H. Son, J.G. Kim, D.H. Hur, Galvanic effect of magnetite 1159 on the corrosion behavior of carbon steel in deaerated alkaline solutions under 1160 flowing conditions, Corros Sci 131 (2018) 71-80. 1161 https://doi.org/10.1016/j.corsci.2017.10.017. 1162 [96] Barry C. Syrett, Otakar Jonas, Joyce M. Mancini, Corrosion in the Condensate-1163 Feedwater System, in: Corrosion: Environments and Industries, ASM 1164 International, 2006: pp. 447-460. 1165 https://doi.org/10.31399/asm.hb.v13c.a0004152. 1166 J. Ducreux, Prediction of Erosion-Corrosion in Steam Water Circuits of Nuclear [97] 1167 Power Plants, 1996. G. Su, Y. Li, J. Zhang, Flow accelerated corrosion and thinning mechanism of the 1168 [98] 1169 pipeline after the butterfly valve based on CFD, Eng Fail Anal 156 (2024) 107844. 1170 https://doi.org/10.1016/j.engfailanal.2023.107844. 1171 T. Xu, R. Zhang, X. Si, Effects of fluid dynamics parameters on flow-accelerated [99] 1172 corrosion at elbow of carbon steel pipeline, Mater Res Express 11 (2024) 056520. 1173 https://doi.org/10.1088/2053-1591/ad4c3c.

1174 1175 1176	[100]	L.B. Boncz, L. Holmegaard, J.L. Sørensen, J. Hald, M.S. Jellesen, Flow-induced corrosion of brass flowmeters used for drinking water, Eng Fail Anal 171 (2025) 109394. https://doi.org/10.1016/j.engfailanal.2025.109394.
1177 1178 1179 1180	[101]	K. Yoneda, T. Ohira, K. Tanji, S. Akiba, K. Niiyama, R. Morita, F. Inada, Evaluation of Hydraulic Factors Affecting Flow Accelerated Corrosion and Its Verification With Power Plant Data, in: Volume 6: Materials and Fabrication, Parts A and B, ASME, Prague, Czech Republic, 2009: pp. 873–879.
1181 1182 1183	[102]	D. Zinemams, A. Herszaz, Flow accelerated corrosion: flow field and mass transport in bifurcations and nozzles, in: International Conference on Water Chemistry for Nuclear Reactor Systems (NPC, Berlin, 2008.
1184 1185 1186 1187 1188	[103]	Masanori Naitoh, Shunsuke Uchida, Seiichi Koshizuka, Hisashi Ninokata, Akihiko Minato, Hiroaki Saitoh, Koji Hotta, Minoru Akiyama, Naoki Anahara, Koji Dozaki, Evaluation Method for Flow Accelerated Corrosion of Components by Corrosion Analysis Coupled with Flow Dynamics Analysis, Heat Transfer Engineering (2010) 712–720.
1189 1190 1191 1192	[104]	Pietralik, John M, B.A.W. Smith, CFD Application to Flow-Accelerated Corrosion in Feeder Bends, in: Volume 4: Computational Fluid Dynamics, Neutronics Methods and Coupled Codes; Student Paper Competition, ASME, Miami, Florida, USA, 2006: pp. 175–185.
1193 1194 1195	[105]	T. Wan, S. Saito, Flow-Accelerated Corrosion of Type 316L Stainless Steel Caused by Turbulent Lead–Bismuth Eutectic Flow, Metals (Basel) 8 (2018) 627. https://doi.org/10.3390/met8080627.
1196 1197 1198 1199	[106]	M.AA. Allah, I. ulhaq Toor, A. Shams, O.K. Siddiqui, Application of Machine Learning and Deep Learning Techniques for Corrosion and Cracks Detection in Nuclear Power Plants: A Review, Arab J Sci Eng 50 (2025) 3017–3045. https://doi.org/10.1007/s13369-024-09388-6.
1200 1201 1202	[107]	Y. Gu, M. Wang, H. Jin, Predictive Study of Flow-Accelerated Corrosion Characteristic Parameters Based on the Neural Network, Corrosion 78 (2022) 751–764. https://doi.org/10.5006/4034.
1203 1204 1205	[108]	A.P. Vélez, M.Z.F. Muñiz, J.L.F. Martínez, Data-driven structural transition detection using vibration monitoring and LSTM networks, AIMS Mathematics 10 (2025) 18558–18585. https://doi.org/10.3934/math.2025829.
1206 1207 1208	[109]	Y.H. Chae, S.G. Kim, H. Kim, J.T. Kim, P.H. Seong, A methodology for diagnosing FAC induced pipe thinning using accelerometers and deep learning models, Ann Nucl Energy 143 (2020) 107501. https://doi.org/10.1016/j.anucene.2020.107501.

1209 1210 1211 1212	[110]	B. Chung, J. Kim, D. Jang, S. Kim, Y. Choi, Experimental investigation of a method for diagnosing wall thinning in an artificially thinned carbon steel elbow based on changes in modal characteristics, Nucl Eng Technol 55 (2023) 947–957. https://doi.org/10.1016/j.net.2022.11.001.		
1213 1214 1215 1216	[111]	JW. Kim, MG. Na, CY. Park, Effect of local wall thinning on the collapse behavior of pipe elbows subjected to a combined internal pressure and in-plane bending load, Nucl Eng Des 238 (2008) 1275–1285. https://doi.org/10.1016/j.nucengdes.2007.10.017.		
1217 1218 1219 1220	[112]	S. Oh, Y. Cheong, D. Kim, K. Kim, On-Line Monitoring of Pipe Wall Thinning by a High Temperature Ultrasonic Waveguide System at the Flow Accelerated Corrosion Proof Facility, Sensors 19 (2019) 1762. https://doi.org/10.3390/s19081762.		
1221 1222 1223 1224	[113]	Yasuyoshi Tomoe, Takashi Ito, Makoto Shimizu, Toshiyuki Sunaba, Inhibitor evaluation for 13%Cr steel in high temperature, sweet conditions, and the effects of co-existence of liquid hydrocarbons, in: Proc. CORROSION 2013, NACE International, 2013.		
1225 1226 1227	[114]	Yuan Ding, Bruce Brown, David Young, Marc Singer, Effectiveness of an Imidazoline-Type Inhibitor Against CO 2 Corrosion of Mild Steel at Elevated Temperatures (120°C-150°C). Corrosion., NACE Corrosion (2018).		
1228 1229 1230	[115]	Jody Hoshowski, Rolando Perez Pineiro, Tore Nordvik, Paul Barnes, Alyn Jenkins, The Development of Novel Corrosion Inhibitors for High Temperature Sour Gas Environments, in: CORROSION 2020, NACE International, 2020.		
1231 1232 1233	[116]	K. Bilkova, N. Hackerman, M. Bartos, Inhibition Effect of Thioglycolic Acid on Carbon Dioxide Corrosion of Carbon Steel, Corrosion 60 (2004) 965–973. https://doi.org/10.5006/1.3287831.		
1234 1235 1236 1237	[117]	F. Farelas, A. Ramirez, Carbon Dioxide Corrosion Inhibition of Carbon Steels Through Bis-imidazoline and Imidazoline Compounds Studied by EIS, Int J Electrochem Sci 5 (2010) 797–814. https://doi.org/10.1016/S1452-3981(23)15324-7.		
1238 1239 1240 1241	[118]	F. Farelas, M. Galicia, B. Brown, S. Nesic, H. Castaneda, Evolution of dissolution processes at the interface of carbon steel corroding in a CO2 environment studied by EIS, Corros Sci 52 (2010) 509–517. https://doi.org/10.1016/j.corsci.2009.10.007.		
1242 1243 1244	[119] D.S. Chauhan, M.A. Quraishi, A. Qurashi, Recent trends in environmentally sustainable Sweet corrosion inhibitors, J Mol Liq 326 (2021) 115117. https://doi.org/10.1016/j.molliq.2020.115117.			

1245 1246 1247	[120]	K. Xhanari, Y. Wang, Z. Yang, M. Finšgar, A Review of Recent Advances in the Inhibition of Sweet Corrosion, The Chemical Record 21 (2021) 1845–1875. https://doi.org/10.1002/tcr.202100072.
1248 1249 1250	[121]	F.F. Eliyan, A. Alfantazi, On the theory of CO2 corrosion reactions – Investigating their interrelation with the corrosion products and API-X100 steel microstructure, Corros Sci 85 (2014) 380–393. https://doi.org/10.1016/j.corsci.2014.04.055.
1251 1252 1253	[122]	Y. Hu, Y.M. Han, L. Xin, Y.H. Lu, The effect of flow velocity and material microstructure on FAC behavior and mechanism in simulated PWR conditions, J Nucl Mater 581 (2023) 154436. https://doi.org/10.1016/j.jnucmat.2023.154436.
1254 1255	[123]	Dharma Abayarathna, Ali Naraghi, Nihal Obeyesekere, Inhibition of Corrosion of Carbon Steel in the Presence of CO2, H2S and S, CORROSION (2003).
1256 1257 1258 1259	[124]	L. Chaal, B. Albinet, C. Deslouis, Y.T. Al-Janabi, A. Pailleret, B. Saidani, G. Schmitt, Wall shear stress mapping in the rotating cage geometry and evaluation of drag reduction efficiency using an electrochemical method, Corros Sci 51 (2009) 1809–1816. https://doi.org/10.1016/j.corsci.2009.05.013.
1260 1261 1262 1263	[125]	Q.H. Zhang, Y.Y. Li, G.Y. Zhu, Y. Lei, X. Wang, H.F. Liu, G.A. Zhang, In-depth insight into the synergistic inhibition mechanism of S-benzyl-L-cysteine and thiourea on the corrosion of carbon steel in the CO2-saturated oilfield produced water, Corros Sci 192 (2021) 109807. https://doi.org/10.1016/j.corsci.2021.109807.
1264 1265 1266 1267	[126]	N.A. Gardner, F.C. Walsh, The Design And Application Of Rotating Cylinder Electrode Technology To Continuous Production Of Metal, in: Electrochemical Cell Design, Springer US, Boston, MA, 1984: pp. 225–258. https://doi.org/10.1007/978-1-4613-2795-0_12.
1268 1269 1270 1271	[127]	G. Kear, B.D. Barker, K.R. Stokes, F.C. Walsh, Corrosion and impressed current cathodic protection of copper-based materials using a bimetallic rotating cylinder electrode (BRCE), Corros Sci 47 (2005) 1694–1705. https://doi.org/10.1016/j.corsci.2004.08.013.
1272 1273	[128]	Raymond B. Goodfellow, Emily Barr, A Case Study of the Design and Operation of a High CO2 Production with H2S., CORROSION (2001).
1274 1275 1276	[129]	S. Ramachandran, V. Jovancicevic, S. Mancuso, C. Menendez, Development of High Shear Corrosion Inhibitor For Mild Steel In Different CO2 And CO2/H2S Environments with and Without Sand, NACE (2011).
1277 1278	[130]	Attila Palencsar, Egil Gulbrandsen, Kateřina Kosorú, High Temperature Testing of Corrosion Inhibitor Performance, CORROSION 2013 (2013).
1279 1280	[131]	Sunder Ramachandran, Vladimir Jovancicevic, Jeff Long, Development of A New Water Soluble High Temperature Corrosion Inhibitor, in: NACE International

1281 1282		Conference, National Association of Corrosion Engineers, Atlanta, Georgia, USA, 2009: pp. 22–26.
1283 1284 1285 1286	[132]	S. Ramachandran, V. Jovancicevic, S. Mancuso, C. Menendez, Development of High Shear Corrosion Inhibitor for Mild Steel in Different CO_2 and $\mathrm{CO}_2/\mathrm{H}_2\mathrm{S}$ Environments with and without Sand, in: CORROSION 2011 (NACE International Conference & Expo), NACE International, 2011.
1287 1288 1289 1290	[133]	Y. Hua, S. Xu, Y. Wang, W. Taleb, J. Sun, L. Zhang, R. Barker, A. Neville, The formation of FeCO3 and Fe3O4 on carbon steel and their protective capabilities against CO2 corrosion at elevated temperature and pressure, Corros Sci 157 (2019) 392–405. https://doi.org/10.1016/j.corsci.2019.06.016.
1291 1292 1293 1294	[134]	A. Shamsa, R. Barker, Y. Hua, E. Barmatov, T.L. Hughes, A. Neville, Impact of corrosion products on performance of imidazoline corrosion inhibitor on X65 carbon steel in CO2 environments, Corros Sci 185 (2021) 109423. https://doi.org/10.1016/j.corsci.2021.109423.
1295 1296 1297	[135]	S. Papavinasam, R.W. Revie, M. Attard, A. Demoz, K. Michaelian, Comparison of Laboratory Methodologies to Evaluate Corrosion Inhibitors for Oil and Gas Pipelines, CORROSION (2003).
1298 1299 1300	[136]	Boyd A. Laurent, Brian M. Bennett, Ryan M. Harrington, Development of Test Methods and Factors for Evaluation of Oilfield Corrosion Inhibitors at High Temperature, CORROSION (2017).
1301 1302 1303	[137]	Sunder Ramachandran, Young Soo Ahn, Michael Greaves, Vladimir Jovancicevic, John Bassett, Development of High Temperature, High Pressure Corrosion Inhibitor, CORROSION 2006 (NACE International Conference & Expo) (2006).
1304 1305 1306 1307	[138]	S. Papavinasam, M. Attard, R.W. Revie, J. Bojes, Rotating Cage - a Compact Laboratory Methodology for Simultaneously Evaluating Corrosion Inhibition and Drag Reducing Properties of Chemicals, in: CORROSION 2002, NACE International, 2002: pp. 1–15. https://doi.org/10.5006/C2002-02271.
1308 1309 1310	[139]	A.H. Alamri, Localized corrosion and mitigation approach of steel materials used in oil and gas pipelines – An overview, Eng Fail Anal 116 (2020) 104735. https://doi.org/10.1016/j.engfailanal.2020.104735.
1311 1312 1313	[140]	M. Askari, M. Aliofkhazraei, R. Jafari, P. Hamghalam, A. Hajizadeh, Downhole corrosion inhibitors for oil and gas production – a review, Applied Surface Science Advances 6 (2021) 100128. https://doi.org/10.1016/j.apsadv.2021.100128.
1314 1315 1316	[141]	T. Kamimura, S. Nasu, T. Segi, T. Tazaki, S. Morimoto, H. Miyuki, Corrosion behavior of steel under wet and dry cycles containing Cr3+ ion, Corros Sci 45 (2003) 1863–1879. https://doi.org/10.1016/S0010-938X(03)00023-4.

1317 1318 1319	[142]	B. Wang, L. Xu, J. Zhu, H. Xiao, M. Lu, Observation and analysis of pseudopassive film on 6.5%Cr steel in CO 2 corrosion environment, Corros Sci 111 (2016) 711–719. https://doi.org/10.1016/j.corsci.2016.06.006.			
1320 1321 1322 1323 1324	[143]	A.A. Rodriguez, J.H. Tylczak, M.C. Gao, P.D. Jablonski, M. Detrois, M. Ziomek-Moroz, J.A. Hawk, Effect of Molybdenum on the Corrosion Behavior of High-Entropy Alloys CoCrFeNi 2 and CoCrFeNi 2 Mo 0.25 under Sodium Chloride Aqueous Conditions, Advances in Materials Science and Engineering 2018 (2018). https://doi.org/10.1155/2018/3016304.			
1325 1326 1327	[144]	X. Hao, J. Dong, J. Wei, II.N. Etim, W. Ke, Effect of Cu on corrosion behavior of low alloy steel under the simulated bottom plate environment of cargo oil tank, Corros Sci 121 (2017) 84–93. https://doi.org/10.1016/j.corsci.2017.03.012.			
1328 1329 1330	[145]	YW. Jang, JH. Hong, JG. Kim, Effects of copper on the corrosion properties of low-alloy steel in an acid-chloride environment, Met Mater Int 15 (2009) 623–629. https://doi.org/10.1007/s12540-009-0623-5.			
1331 1332 1333	[146]	L. Xu, B. Wang, J. Zhu, W. Li, Z. Zheng, Effect of Cr content on the corrosion performance of low-Cr alloy steel in a CO2 environment, Appl Surf Sci 379 (39–46. https://doi.org/10.1016/j.apsusc.2016.04.049.			
1334 1335 1336 1337	[147]	J. Zhou, L. Ren, Y. Lv, W. Lin, W. Jian, D. Zhang, X. Suo, D. Ruan, Q. Zhang, Investigation on the component prediction and supercritical water oxidation Ni-Cr-Mo alloy based on machine learning, J Nucl Mater 605 (2025) 155566. https://doi.org/10.1016/j.jnucmat.2024.155566.			
1338 1339 1340 1341	[148]	Z. Zhan, X. Huang, Q. Zhao, J. Liu, L. Wei, X. Li, Effect of oxygen concentrations on the corrosion behavior of a duplex-phase FeNiCrCuAl high entropy alloy in supercritical water, J Nucl Mater 572 (2022) 154046. https://doi.org/10.1016/j.jnucmat.2022.154046.			
1342 1343 1344 1345	[149]	Z. Wang, Y. Yan, Y. Wu, Y. Zhang, X. Zhao, Y. Su, L. Qiao, Recent research progress on the passivation and selective oxidation for the 3d-transition-metal and refractory multi-principal element alloys, Npj Mater Degrad 7 (2023) 86. https://doi.org/10.1038/s41529-023-00410-0.			
1346 1347 1348	[150]	E. Chajduk, A. Bojanowska-Czajka, Corrosion mitigation in coolant systems in nuclear power plants, Prog Nucl Energy 88 (2016) 1–9. https://doi.org/10.1016/j.pnucene.2015.11.011.			
1349 1350 1351	[151]	1] D. Jero, N. Caussé, N. Pébère, Film-forming amines as corrosion inhibitors: a state-of-the-art review, Npj Mater Degrad 8 (2024) 111. https://doi.org/10.1038/s41529-024-00523-0.			

1352 1353 1354	[152]	C. Liu, G. Lin, Y. Sun, J. Lu, J. Fang, C. Yu, L. Chi, K. Sun, Effect of octadecylamine concentration on adsorption on carbon steel surface, Nucl Eng Technol 52 (2020) 2394–2401. https://doi.org/10.1016/j.net.2020.03.026.
1355 1356 1357 1358	[153]	S. Weerakul, N. Leaukosol, D.H. Lister, S. Mori, W. Hater, Effects on Flow-Accelerated Corrosion of Oleylpropanediamine Under Single-Phase Water Conditions Pertinent to Power Plant Feedwater, Corrosion 76 (2020) 217–230. https://doi.org/10.5006/3225.
1359 1360 1361	[154]	H. Verbruggen, K. Baert, H. Terryn, I. De Graeve, Molybdate-phosphate conversion coatings to protect steel in a simulated concrete pore solution, Surf Coat Technol 361 (2019) 280–291. https://doi.org/10.1016/j.surfcoat.2018.09.056.
1362 1363 1364 1365	[155]	O.O. Joseph, S. Sivaprasad, O.S.I. Fayomi, Comparative study on the effect of NaNO 2 in corrosion inhibition of micro-alloyed and API-5L X65 steels in E20 simulated FGE, Energy Procedia 119 (2017) 953–960. https://doi.org/10.1016/j.egypro.2017.07.128.
1366 1367 1368	[156]	R.S. Pathania, E.G. McVey, Evaluation of Sodium Phosphate as A Denting Inhibitor, Nucl Technol 55 (1981) 178–190. https://doi.org/10.13182/NT81-A32840.
1369 1370 1371 1372 1373	[157]	K. Patra, V.K. Mittal, T.P. Valsala, S. Bera, A.K. Sahu, D.B. Sathe, R.B. Bhatt, Corrosion and contamination study of nuclear plant steel in HNO3-Based waste solution with Strontium under nuclear processing environment, Journal of Hazardous Materials Advances 13 (2024) 100399. https://doi.org/10.1016/j.hazadv.2023.100399.
1374 1375	[158]	P.C. Wu, Erosion/Corrosion-Induced Pipe Wall Thinning in U.S. Nuclear Power Plants, U.S. Department of Energy, 1989. https://doi.org/10.2172/6152848.
1376 1377 1378	[159]	XX. Yuan, M.D. Pandey, G.A. Bickel, A probabilistic model of wall thinning in CANDU feeders due to flow-accelerated corrosion, Nucl Eng Des 238 (2008) 16–24. https://doi.org/10.1016/j.nucengdes.2007.06.004.
1379 1380 1381	[160]	E. Bismut, M.D. Pandey, D. Straub, Reliability-based inspection and maintenance planning of a nuclear feeder piping system, Reliab Eng Syst Saf 224 (2022) 108521. https://doi.org/10.1016/j.ress.2022.108521.
1382 1383 1384	[161]	J. Luque, D. Straub, Risk-based optimal inspection strategies for structural systems using dynamic Bayesian networks, Structural Safety 76 (2019) 68–80. https://doi.org/10.1016/j.strusafe.2018.08.002.
1385 1386 1387	[162]	E. Bismut, D. Straub, Optimal adaptive inspection and maintenance planning for deteriorating structural systems, Reliab Eng Syst Saf 215 (2021) 107891. https://doi.org/10.1016/j.ress.2021.107891.

1388 [163] S. Alaswad, Y. Xiang, A review on condition-based maintenance optimization 1389 models for stochastically deteriorating system, Reliab Eng Syst Saf 157 (2017) 54– 1390 63. https://doi.org/10.1016/j.ress.2016.08.009. 1391 [164] Y. Wang, X. Li, J. Chen, Y. Liu, A condition-based maintenance policy for multi-1392 component systems subject to stochastic and economic dependencies, Reliab 1393 Eng Syst Saf 219 (2022) 108174. https://doi.org/10.1016/j.ress.2021.108174. 1394 [165] S. Bressi, J. Santos, M. Losa, Optimization of maintenance strategies for railway 1395 track-bed considering probabilistic degradation models and different reliability 1396 levels, Reliab Eng Syst Saf 207 (2021) 107359. 1397 https://doi.org/10.1016/j.ress.2020.107359. 1398 [166] W.H. Ahmed, Evaluation of the proximity effect on flow-accelerated corrosion, 1399 Ann Nucl Energy 37 (2010) 598-605. 1400 https://doi.org/10.1016/j.anucene.2009.12.020. 1401 [167] Y.Z. Shen, S.H. Kim, H.D. Cho, C.H. Han, W.S. Ryu, Precipitate phases of a 1402 ferritic/martensitic 9% Cr steel for nuclear power reactors, Nucl Eng Des 239 1403 (2009) 648-654. https://doi.org/10.1016/j.nucengdes.2008.12.018. 1404 [168] G. Zheng, L. He, D. Carpenter, K. Sridharan, Corrosion-induced microstructural 1405 developments in 316 stainless steel during exposure to molten Li2BeF4(FLiBe) 1406 salt, J Nucl Mater 482 (2016) 147-155. 1407 https://doi.org/10.1016/j.jnucmat.2016.10.023. 1408 [169] C. Nash, P. Karve, D. Adams, Diagnosing nuclear power plant pipe wall thinning 1409 due to flow accelerated corrosion using a passive, thermal non-destructive 1410 evaluation method: Feasibility assessment via numerical experiments, Nucl Eng 1411 Des 386 (2022) 111542. https://doi.org/10.1016/j.nucengdes.2021.111542. 1412 [170] P. Huthwaite, R. Ribichini, P. Cawley, M.J.S. Lowe, Mode selection for corrosion 1413 detection in pipes and vessels via guided wave tomography, IEEE Trans Ultrason 1414 Ferroelectr Freq Control 60 (2013) 1165-1177. https://doi.org/10.1109/TUFFC.2013.2679. 1415 1416 [171] H.R. Vanaei, A. Eslami, A. Egbewande, A review on pipeline corrosion, in-line 1417 inspection (ILI), and corrosion growth rate models, International Journal of 1418 Pressure Vessels and Piping 149 (2017) 43-54. 1419 https://doi.org/10.1016/j.ijpvp.2016.11.007. 1420 [172] L.B. Coelho, D. Zhang, Y. Van Ingelgem, D. Steckelmacher, A. Nowé, H. Terryn, 1421 Reviewing machine learning of corrosion prediction in a data-oriented 1422 perspective, Npj Mater Degrad 6 (2022) 8. https://doi.org/10.1038/s41529-022-1423 00218-4.

1424 1425 1426	[173]	K. Ranjbar, Effect of flow induced corrosion and erosion on failure of a tubular heat exchanger, Mater Des 31 (2010) 613–619. https://doi.org/10.1016/j.matdes.2009.06.025.	
1427 1428 1429 1430	[174]	K. YONEDA, K. FUJIWARA, R. MORITA, F. INADA, Development of flow-accelerated corrosion prediction method (2) Modeling and validation with thinning rate profile data, Mechanical Engineering Journal 5 (2018) 17-00415-17–00415. https://doi.org/10.1299/mej.17-00415.	
1431 1432 1433	[175]	D.C. Sweeney, A.M. Schrell, C.M. Petrie, Pressure-Driven Fiber-Optic Sensor for Online Corrosion Monitoring, IEEE Trans Instrum Meas 70 (2021) 1–10. https://doi.org/10.1109/TIM.2021.3089231.	
1434 1435 1436	[176]	M. Hren, T. Kosec, M. Lindgren, E. Huttunen-Saarivirta, A. Legat, Sensor Development for Corrosion Monitoring of Stainless Steels in H2SO4 Solutions, Sensors 21 (2021) 1449. https://doi.org/10.3390/s21041449.	
1437 1438 1439	[177]	P.R. Ohodnicki, M. Ziomek-Moroz, Corrosion proxy material integrated sensor devices for distributed sensing of early corrosion onset and corrosion quantification, U.S. Patent 11,262,289, 2022.	
1440 1441 1442 1443	[178]	W. Tian, J. Deng, S.A. Higazy, M.S. Selim, H. Jin, Self-Healing Anti-Corrosion Coatings: Challenges and Opportunities from Laboratory Breakthroughs to Industrial Realization, Coatings 15 (2025) 620. https://doi.org/10.3390/coatings15060620.	
1444 1445 1446	[179]	J. Zhang, Long-Term Behaviors of Oxide Layer in Liquid Lead–Bismuth Eutectic (LBE), Part I: Model Development and Validation, Oxidation of Metals 80 (2013) 669–685. https://doi.org/10.1007/s11085-013-9450-7.	
1447 1448 1449 1450	[180]	K. Yoneda, R. Morita, K. Fujiwara, F. Inada, Development of flow-accelerated corrosion prediction method (1) Acquisition of basic experimental data including low temperature condition, Mechanical Engineering Journal 3 (2016) 15-00232-15–00232. https://doi.org/10.1299/mej.15-00232.	
1451 1452 1453 1454	[181]	K. Das, T. Mintz, D. Basu, Numerical Evaluation of Corrosion Condition for Pressurized Water Reactor Secondary Cooling System, in: Volume 5: High- Pressure Technology; Nondestructive Evaluation; Nuclear Engineering, ASMEDC, 2011: pp. 293–302. https://doi.org/10.1115/PVP2011-57819.	
1455 1456	[182]	F.N. Remy, M. Bouchacourt, Flow-assisted corrosion: a method to avoid damage, Nucl Eng Des 133 (1992) 23–30. https://doi.org/10.1016/0029-5493(92)90084-9.	
1457 1458 1459	[183]	3] K. Yoneda, Evaluation of hydraulic factors affecting flow-accelerated corrosion and its verification with power plant data, in: ASME 2009 Pressure Vessels and Piping Conference (PVP), ASME, Prague, 2009.	

1460 1461 1462	[184]	in: Nuclear Corrosion Science and Engineering, Elsevier, 2012: pp. 57–74. https://doi.org/10.1533/9780857095343.1.57.
1463 1464 1465 1466 1467 1468	[185]	P. Madasamy, H. Subramanian, T. V Krishna Mohan, S. Velmurugan, E. Natarajan, S. V Narasimhan, Experimental determination of flow accelerated corrosion in bend and straight sections of carbon steel primary coolant feeder pipes in pressurised heavy water reactor system, Corrosion Engineering, Science and Technology 46 (2011) 346–352. https://doi.org/10.1179/147842209X12476568584502.
1469 1470 1471	[186]	Y. Utanohara, Y. Nagaya, A. Nakamura, M. Murase, Influence of Local Flow Field on Flow Accelerated Corrosion Downstream from an Orifice, Journal of Power and Energy Systems 6 (2012) 18–33. https://doi.org/10.1299/jpes.6.18.
1472 1473 1474 1475	[187]	Y. Hu, L. Xin, C. Hong, Y. Han, Y. Lu, Microstructural Understanding of Flow Accelerated Corrosion of SA106B Carbon Steel in High-Temperature Water with Different Flow Velocities, Materials 16 (2023) 3981. https://doi.org/10.3390/ma16113981.
1476 1477 1478	[188]	L. Zeng, G. Chen, H. Chen, Comparative Study on Flow-Accelerated Corrosion and Erosion–Corrosion at a 90° Carbon Steel Bend, Materials 13 (2020) 1780. https://doi.org/10.3390/ma13071780.
1479 1480 1481 1482	[189]	L. Yang, D. Zhang, H. Fan, X. Fu, R. Yan, Z. Wei, H. Wu, In-situ electrochemical testing and fluid dynamics simulation of pipeline defects under flow accelerated corrosion, Exp Therm Fluid Sci 150 (2024) 111048. https://doi.org/10.1016/j.expthermflusci.2023.111048.
1483 1484 1485 1486	[190]	J. Cao, T. Ma, D. Li, Z. Li, J. Shi, L. Zeng, H. Chen, Unveiling the inhibition of high-pressure CO2 flow accelerated corrosion at gradual contraction and gradual expansion tubings, Corros Sci 239 (2024) 112375. https://doi.org/10.1016/j.corsci.2024.112375.
1487		
1488		
1489		
1490	List o	f Tables

Table 1: Environmental and material factors influencing FAC.

Parameter	Effect on FAC	Ref
Temperature (120–180 °C, peak near 150 °C)	Magnetite solubility maximized, accelerating FAC	[53]

Low pH / Low ORP	Promotes oxide instability	[22]
Low dissolved oxygen	Enhance electrochemical reaction rates	[44]
Material (Cr, Cu alloys)	Improves oxide stability, resists Fac	[38], [184]

Table 2: List of major international FAC incidents in nuclear power plants.

Plant/Country	Year	Break Point
Saint-Laurent A2, France	1972	Straight pipe downstream of orifice (SG).
Oconee-3, USA	1976	Extraction line.
Trojan, USA	1985	Feedwater heater / piping.
Surry-2, USA	1986	Feedwater elbow rupture (fatal accident).
Santa Maria de Garoña, Spain	1989	Steam line rupture inside containment.
Loviisa-1, Finland	1990	Feedwater line downstream of orifice.
Almaraz-1, Spain	1991	SG tube inlet with orifice (AVT water).
Fort Calhoun, USA	1997	Steam piping (elbow rupture).
Mihama-3, Japan	2004	Condensate water pipe after orifice (fatal rupture).
Zaporozhye-4, Ukraine	2004	Straight pipe downstream of elbow.
Bruce-8, Canada	2003	SG tube support plate thinning.
South Ukraine-2, Russia	2005	Moisture separator drain line.
Kakrapar-2, India	2006	Feedwater straight pipe downstream of orifice.
Karashi, Pakistan	2007	Small drain line from HP turbine.
Davis-Besse, USA	2015	4-inch pipe in moisture separator reheater system (steam leak, FAC thinning).
Indian Point Unit 3, USA	2018	6-inch elbow upstream of 36C feedwater heater (steam leak, FAC thinning).

1498 Table 3: Summary of the previous studies related to FAC outlining the main findings.

Author	Method	Type of Steel	Section in NPP	Main parameters	Observations and comments
Kim et al. [23]	Experimental (HTHP rotating cage autoclave)	Commercial A516 Gr.60 (0.04% Cr, Mo-free), P22 (2.25Cr–1Mo), and model alloys: FRA1 (2.25Cr– 1Mo), FRA2 (3.2Cr– 0.5Mo), MFRA (4.2Cr, Mo-free)	Secondary side of pressurized water reactors (PWR feed water environment simulated)	T = 150 °C; P = 8 MPa; pH = 9.3; DO < 1 ppb; Flow velocity = 5.7 m/s; Exposure time = 14 days; Chromium content and Molybdenum content.	 FAC resistance mainly depends on Cr content in oxide films, while Mo has negligible effect on uniform FAC. Alloys with higher Cr (≥3 wt.%) showed lower FAC rates.
Yoneda et al. [180]	Experimental (PRINTEMPS loop)	Carbon steel JIS STPT480 (Cr \~0.001 wt%	Condensate demineralizer downstream and deaerator upstream sections of the PWR feed water system	Temperature: 50–150 °C; pH: 7.0–9.8; Velocity: 1.5– 10 m/s; Contraction height: 0–3 mm; DO < 1 ppb.	 FAC rate peaks at 150 °C but remains notable even at 50 °C. A significant decrease in FAC rate is observed around pH 9.0. FAC rate increases with flow velocity (v^1.0-1.5), with magnetite as the main oxide formed.
Utanohara & Murase [55]	Experimental (HTHP recirculating loop)+CFD comparison of flow field	Carbon steel STPT42 (Ni 0.02 wt%, Cr 0.04 wt%, Mo 0.01 wt%)	Elbow section (D = 49.5 mm, horizontal plane bend)	Velocity: 0.39–5.74 m/s; Temperature: 50–150 °C; Pressure: 1.5 MPa; DO < 0.1 μg/kg; Neutral pH \~7; Exposure time 78–1624 h	 FAC at elbow 1.7–2.9× higher than upstream. At 150 °C intrados least susceptible; at 100 °C intrados most susceptible; FAC still present at 50 °C (~0.09 mm/y). Nonlinear velocity dependence (exp. 1.0–2.3); strong T–v coupling governs FAC, most critical at elbow.
Moon et al. [61]	Experimental + CFD (FAC loop with elbow sections +ANSYS Fluent CFD with k- ε turbulence model)	SA106 Gr. B carbon steel (C 0.19%, Mn 0.98%, Si 0.24%, Cr 0.04%, Ni 0.02%, Mo 0.01%)	Elbow sections of secondary piping in PWR feedwater system	Flow velocity: 9 m/s; Temperature: 150 °C; Pressure: 10 atm; Dissolved oxygen < 5 ppb; pH = 7 (neutral); Exposure: 884 h; Thickness measured at 88 locations (intrados, extrados, upstream/downstream)	 Wall thinning was greatest at the intrados (~0.28 mm/y) compared to the extrados (~0.20–0.23 mm/y). CFD showed peak wall shear stress and turbulence intensity coincided with maximum thinning zones (≈3–9 o'clock). Shear stress and turbulence intensity identified as reliable predictors of FAC-susceptible regions, aiding inspection planning.
Wang et al. [69]	Experimental (Rotating Cylinder Electrode, RCE) + Wet gas flow loop tests	Carbon steel vs. 3Cr low- alloy steel (≈ 3 wt% Cr)	Relevant to high-flow wet gas pipeline environments (simulated extreme wall shear conditions)	Wall shear stress up to 212 Pa, High flow rate conditions,Comparison of corrosion film stability	 Pure carbon steel: FeCO₃ film unstable and easily damaged under high shear → poor protection. 3Cr steel: formation of mixed Cr(OH)₃ + FeCO₃ film, denser and more protective even at high flow/shear.

(FeCO ₃ vs. Cr(OH) ₃ +
FeCO ₃)

 Chromium additions significantly enhanced FAC resistance under extreme hydrodynamic conditions.

Chae et al. [109]	Experimental + Data-driven modeling (FAC test-bed loop with accelerometers, vibration signal analysis; ML: SVM, CNN, LSTM)	Carbon steel pipes (low- Cr, simulating secondary loop piping)	Secondary loop of nuclear power plants (FAC-prone elbows and U-tubes)	T = 120 °C; P = 20 bar; pH = 4; DO controlled; Vibration data at 20 kHz from 3-axis accelerometers.
Kim et al. [111]	Numerical (3D nonlinear finite element analysis, elastic–plastic FE model in ABAQUS).	Pipe elbows modeled as carbon steel (yield stress 302 MPa, ultimate 452 MPa, $E = 206$ GPa, $v = 0.3$)	Nuclear piping elbows subjected to internal pressure + in-plane bending	Geometry + load impact
Oh et al. [112]	Experimental (Development and application of a high- temperature ultrasonic waveguide system for online monitoring)	Carbon steel piping (SA106B equivalent, used in secondary loop	Secondary-side piping of NPPs (feedwater/condensate systems)	T up to 250 °C; P \~15 MPa; pH neutral to alkaline (8– 9.5); Dissolved oxygen <10 ppb.
Tomoe et al. [113]	Experimental (HTHP Hastelloy C-276 lined autoclave with chemical injection device)	13%Cr martensitic stainless-steel tubing (API- 13Cr, C 0.20%, Cr 13.0%, Ni 0.08%, Mo 0.02%)	Simulated hot sweet gas gathering lines (wellhead to choke, >130 °C)	$T=135$ °C and 150 °C; $P=3.1-3.3$ MPa CO ₂ -saturated brine; Cl ⁻ = 1000 mg/L; Acetic acid = 600 μ L/L; Inhibitors: C ₁₂ amines, C ₁₂ carboxylates, C ₁₈

- For chemically FAC-thinned pipes, vibration mode changes were subtle and difficult to distinguish.
- Conventional ML methods (SVM, CNN) had low accuracy (<40%), while LSTM deep learning achieved ~96% by capturing time dependencies.
- Demonstrated potential of vibration + AI for real-time FAC thinning diagnosis, though interpretability and generalization remain challenges.
- Collapse integrity was most affected by thinning at the intrados compared to the extrados.
- Shallow thinning reduced collapse moment nearly linearly with defect size, while deeper thinning caused nonlinear (parabolic/exponential) reductions.
- Failure modes were local buckling under compression and plastic collapse under tension, with larger bend radii increasing sensitivity.
- Detected FAC-induced thinning in real time using a stable ultrasonic waveguide sensor.
- Sensor operated reliably in high-temperature water (up to 250 °C) for >1000 h with stable signal quality.
- Enabled non-intrusive, online monitoring of thinning rates (0.1– 0.3 mm/year) under simulated secondary loop conditions.
- Carboxylates provided much higher inhibition efficiency than amines on 13%Cr steel.
- Addition of hydrocarbons (e.g., xylene) greatly enhanced inhibitor performance, showing strong carboxylate-hydrocarbon synergy.
- Commercial inhibitors were most effective, with efficiency strongly dependent on hydrocarbon presence.

carboxylates (stearic, oleic,

linoleic, linolenic), Ndodecanoylsarcosinate, and commercial A & B;

				With/without xylene (hydrocarbon)	
Ding et al. [114]	Experimental (HTHP single- and two-autoclave systems)	API 5L X65 carbon steel (C 0.13%, Mn 1.16%, Si 0.26%, Mo 0.16%, Ni 0.36%)	Simulated CO ₂ -rich secondary-side piping conditions	T = 120 °C and 150 °C; P = 2 bar pCO ₂ ; Electrolyte: 1 wt.% NaCl saturated with CO ₂ ; Initial pH = 4.3 (at 80 °C); Inhibitor = diethylenetriamine tall oil fatty acid imidazoline (DETA/TOFA imidazoline), 440–880 ppm; Impeller speed = 200 rpm; Exposure = 24 h	 Imidazoline inhibitor was effective at 120 °C (~61% efficiency) but failed at 150 °C. Thermal degradation and Fe₃O₄ formation limited protection, making it unreliable above 150 °C.
Hoshowski et al. [115]	Experimental (HTHP autoclave testing with weightloss coupons)	Carbon steel AISI 1018 (baseline test metal)	Representative of sour service pipelines and well tubulars (high T, CO ₂ + H ₂ S)	T = 140 °C (Middle East), 150 °C (Gulf of Mexico), 177 °C (South Texas); pCO ₂ = 38–160 psi; pH ₂ S = 0.065– 54 psi; Simulated brines (high salinity, up to 214,736 mg/L Cl ⁻); Inhibitors tested: Formulation A (imidazoline + pyrimidine), B (pyrimidine-based), C (pyrimidine + sulfur synergist); Exposure = 3 days	 Effectiveness of traditional imidazoline inhibitors dropped above 150 °C. Pyrimidine-based formulations provided persistent, uniform protection at high temperatures and sour conditions.
Laurent et al. [136]	Experimental (Rotating Cage Autoclave, RCA)	API 5L X65 pipeline steel coupons	Simulated feed water/pipeline environments under HTHP	**Condition A:** T = 135– 149 °C, pCO ₂ = 36 psi, NaCl-dominated brine A (214 g/L Cl ⁻), 10% hydrocarbon phase, 815 rpm, 7 d. **Condition B:** T = 177–204 °C, pCO ₂ = 40 psi, pH ₂ S = 0.32 psi, brine B (139 g/L Cl ⁻), 10% hydrocarbon, 1060 rpm, 7 days.	 Efficiency strongly influenced by scale formation and Fe²⁺ saturation in closed-cell testing. Scale inhibitors (SI) altered results significantly, sometimes increasing corrosion by >5×. Pyrimidine-based inhibitors outperformed imidazolines under severe high-T/sour brine conditions.

Ramachandran et al. [137]	Experimental (High-Speed Autoclave Test, HSAT)	AISI 1018 carbon steel coupons (11.3 cm² exposed surface per coupon)	Simulated high- temperature CO ₂ -rich sour gas wells.	Various inhibitors under different operating conditions	 Shear and temperature dependent performance observed across inhibitors. Inhibitor D (imidazoline–surfactant) showed best stability and efficiency >92% under extreme HTHP conditions.
Xu et al. [146]	Experimental (HTHP autoclave)	Low-alloy steels with 1%, 2%, 3%, 4%, 5%, and 6.5% Cr; comparison with pipeline steel X65	Representative of CO ₂ -rich secondary-side environments (oil & gas / NPP relevant piping)	T = 80 °C; P = 0.8 MPa CO_2 - saturated brine (simulated formation water); pH = 5.57 (CO_2 sat.); Flow = 228 rpm specimen rotation; Exposure = 120 h	 Cr(OH)₃ films enhanced corrosion resistance through spontaneous prepassivation at ≥3% Cr. Steels with <3% Cr showed only active dissolution without protective film formation.
Madasamy et al [186]	Experimental (HTHP loop with custom FAC module)	Carbon steel ASTM A106 Gr. B	Primary coolant feeder pipes of PHWR (outlet bend and straight section)	Velocity: 13.5–20 m/s; Temperature: 270 °C and 284 °C; Pressure: 8.2–11 MPa; pH ≈ 10.2 (LiOH); DO < 10 ppb; Exposure: 75 days	 Increase in corrosion by 2.5 times in bent compared to the straight. Both the ends of the bent and straight sections exhibited relatively high corrosion rates.
Yoneda et al. [174]	Modeling (FAC prediction method with CFD-based effective mass transfer coefficient)	Carbon steel JIS STPT480 (Cr ~0.001 wt%)	Feedwater and condensate piping systems, including elbows and contracted flow sections	Temperature: 50–150 °C; pH: 7.0–9.8; Velocity: 1.5– 4.5 m/s; Contraction height: 3 mm; DO < 1 ppb	 The experimental and predicted FAC rates showed good agreement (velocity exponent α ≈ 0.88). Model validation against plant elbows (~93% conservative) confirmed reliability across both low- and high-temperature conditions.
Utanohara et al. [187]	Experimental (HTHP water loop with orifice test section + CFD validation with LES & RANS)	Carbon steel STPT42 (Cr ~0.04 wt%, Ni 0.02 wt%, Mo 0.01 wt%)	Downstream of orifice in recirculating piping	Velocity was changed from 1.4 to 5 m/s; Temperature: 150 °C; Pressure: 1.5 MPa; DO < 0.1 ppb; pH 5.8–6.2; Exposure time 116 h	 The maximum FAC rate appeared at 1D or 2D and gradually reduced downstream at 3D and 4D. RMS wall shear stress correlated best with FAC distribution, especially at the reattachment zone (~2.5D).
Hu et al. [188]	Experimental (High- temperature water rotating- cylinder electrode system)	Carbon steel SA106B (C 0.21 wt%, Mn 0.53 wt%, Si 0.26 wt%, Cr 0.02 wt%)	Secondary side piping of pressurized water reactors (simulated feedwater environment	Flow velocity: 0, 1.63, 2.99, 4.34 m/s; T = 290 °C; P = 10 MPa; pH = 9.7 (ammonia adjusted); DO < 10 ppb; Exposure = 720 h	 FAC rates increased linearly with flow velocity, but normalization reduced rates by ~20-33%. Microstructural heterogeneity (ferrite-pearlite, Fe₃C/ferrite interfaces) promoted localized corrosion, which was mitigated by refined pearlite spacing after normalizing.
Zeng et al. [189]	Experimental (Closed-loop flow rig with 90° bend)	API X65 pipeline steel (C 0.04%, Si 0.20%, Mn 1.5%, P 0.011%, S 0.003%, Mo 0.02%)	90° carbon steel bend (representative of elbows in pipelines/power plant feedwater)	Flow velocity: 4 m/s; T = 60 °C; CO ₂ -saturated brine simulating produced water (NaCl, KCl, CaCl ₂ , Na ₂ SO ₄ , MgCl ₂ , NaHCO ₃); Pressure 1	The inside wall (intrados) suffered more severe corrosion under FAC, while the outside wall (extrados) was more damaged under E–C with sand.

				bar; Exposure: 8 h; With/without sand (0.29 wt%, 400–500 μm)	Hydrodynamics controlled the damage mechanism: shear/mass transfer for FAC vs. particle impact for E–C.
Yang et al. [190]	Experimental + Numerical (Micro-visualization FAC loop with high-shear channel +CFD/COMSOL for flow simulation)	API X65 pipeline steel (C 0.083%, Mn 1.48%, Si 0.20%, Cr 0.12%, Ni 0.013%, Mo 0.002%)	Pipeline defects: depression (4 mm wide × 1.2 mm deep) and welded joints with weld reinforcement (10 mm wide × 1.2 mm high)	Flow velocity = 5 m/s; T = 45 ± 1 °C; CO ₂ -saturated NACE brine (pH 2.76–2.90); Exposure up to 12 h	 Swirling vortices and jet impacts at weld reinforcements intensified localized FAC. Depressions and weld HAZ acted as hot-spots due to high shear stress and turbulence—mass transfer coupling.

Table 4: Comparative summary of corrosion testing methods, including flow parameters (Reynolds numbers), advantages, limitations, materials tested, and operating conditions.

Method	Flow / Re (rpm or m/s)	Advantages	Limitations	Materials	Operating conditions (temperature & pressure or shear)	Reference(s)
Stirred Autoclave	300– 500 rpm (impeller speed).	 Widely used for corrosion tests. Maintains well-mixed solution even at high T/P. Simple setup can accommodate multiple coupons. 	 Poor simulation of high flow/high-shear conditions. Only single-phase. 	 Carbon steels (mild steel, AISI 1018, API X65) and 13%Cr stainless steel. 	 Up to 300 °C and 35 MPa. in advanced systems (typical tests at 120–177 °C and 0.3–1.1 MPa CO₂). 	Ding et al. [112], Hoshowski et al. [115].
Rotating Cylinder Electrode (RCE)	Up to 2000 rpm (Re $\approx 10^{5}$).	 Uniform turbulent flow with controlled shear. High mass-transfer rates. Allows in-situ corrosion rate monitoring. Compact design (small volume, no large flow loop). 	 Cannot fully simulate realistic gas mixtures or multiphase flow. Test geometry differs from actual pipe flow. 	 Carbon steel cylinders (e.g. mild steel, pipeline steels). 	 Typically, 20–80 °C, 1 atm in lab tests. Specialized autoclave RCE setups up to 300 °C and 350 bar for high-CO₂ environments. 	Gardner and Walsh [126], Kear et al. [127].
Rotating Disk Electrode (RDE)	500 rpm (laminar flow).	 Quick and low-cost method for screening. Well-defined laminar hydrodynamics useful for fundamental studies. 	 Laminar flow pattern not representative of turbulent pipe conditions. Limited mass transfer compared to turbulent systems. 	• Typically, carbon steel disk electrodes (e.g. pipeline steel alloys).	• Employed in high-T/P autoclave tests (e.g. CO ₂ -saturated water at 135 °C, 1 MPa for 24 h).	Chaal et al. [124], Zhang et al., [125].
Jet Impingement	2–6 m/s fluid jet.	 Generates high local shear stress. 	 Highly localized impact zone. Difficult to use for evaluating corrosion 	• Carbon steel coupons (e.g. API 5L X65, AISI 1018) in	• 0–150 °C, 0.5–5.5 bar CO ₂ in tests.	Palencsár et al. [130], Ramachandran et al. [137].

Method	Flow / Re (rpm or m/s)	Advantages	Limitations	Materials	Operating conditions (temperature & pressure or Reference(s) shear)
		 It is widely used to study flow-induced (turbulent) corrosion and erosion effects. (Mimics aggressive flow at pipe elbows, etc.). 	inhibitors (protective films often disrupted).	single- or multiphase flow.	• wall shear stress 100–200 Pa under high-velocity flow.

List of Figures

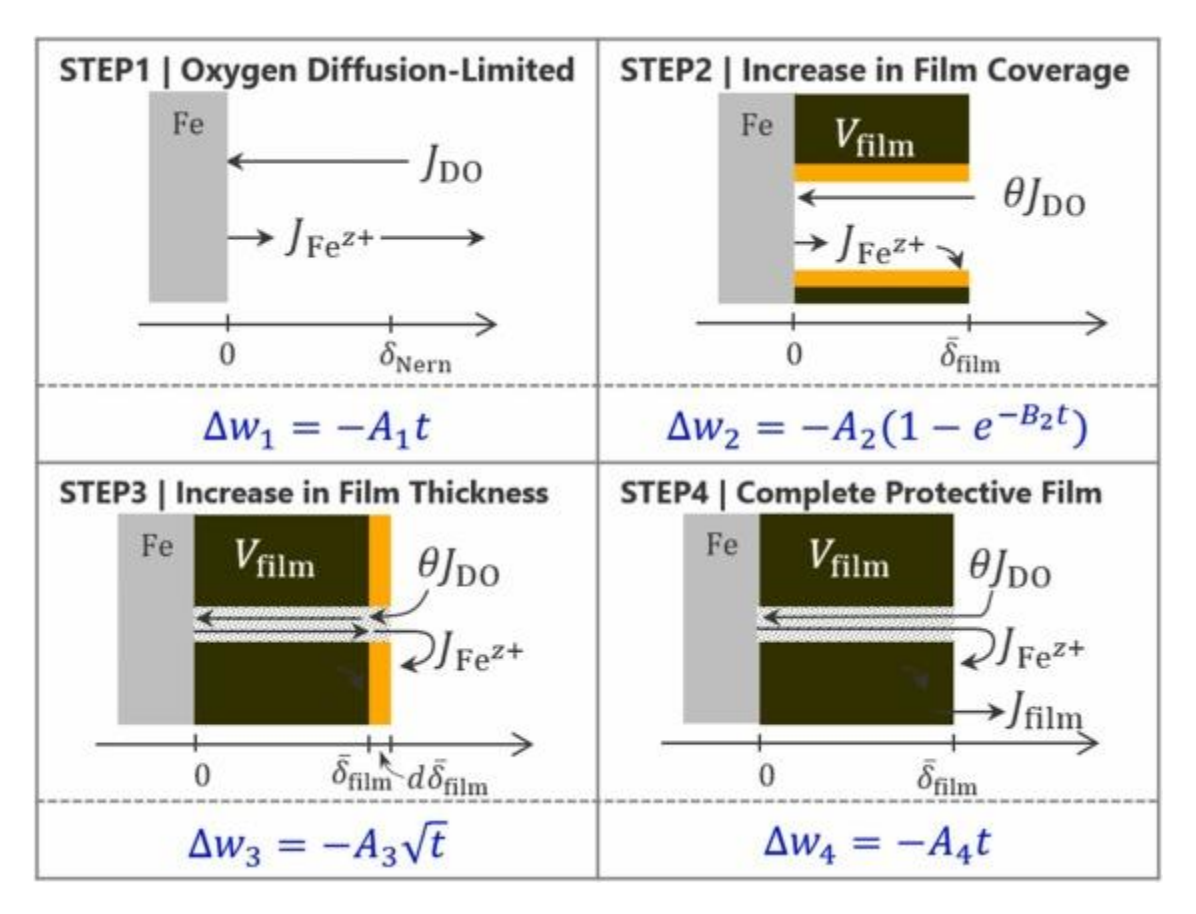


Figure 1: Four-step model of oxide film formation on carbon steel: (Step 1) Oxygen diffusion-limited dissolution; (Step 2) partial film coverage; (Step 3) Thickening of the protective layer; (Step 4) Completion of the film with active ion diffusion paths. Orange shading shows film growth direction; transport of Fe²⁺ and O₂ remains possible within the structure. (Reprinted from references [43] with copyright permission).

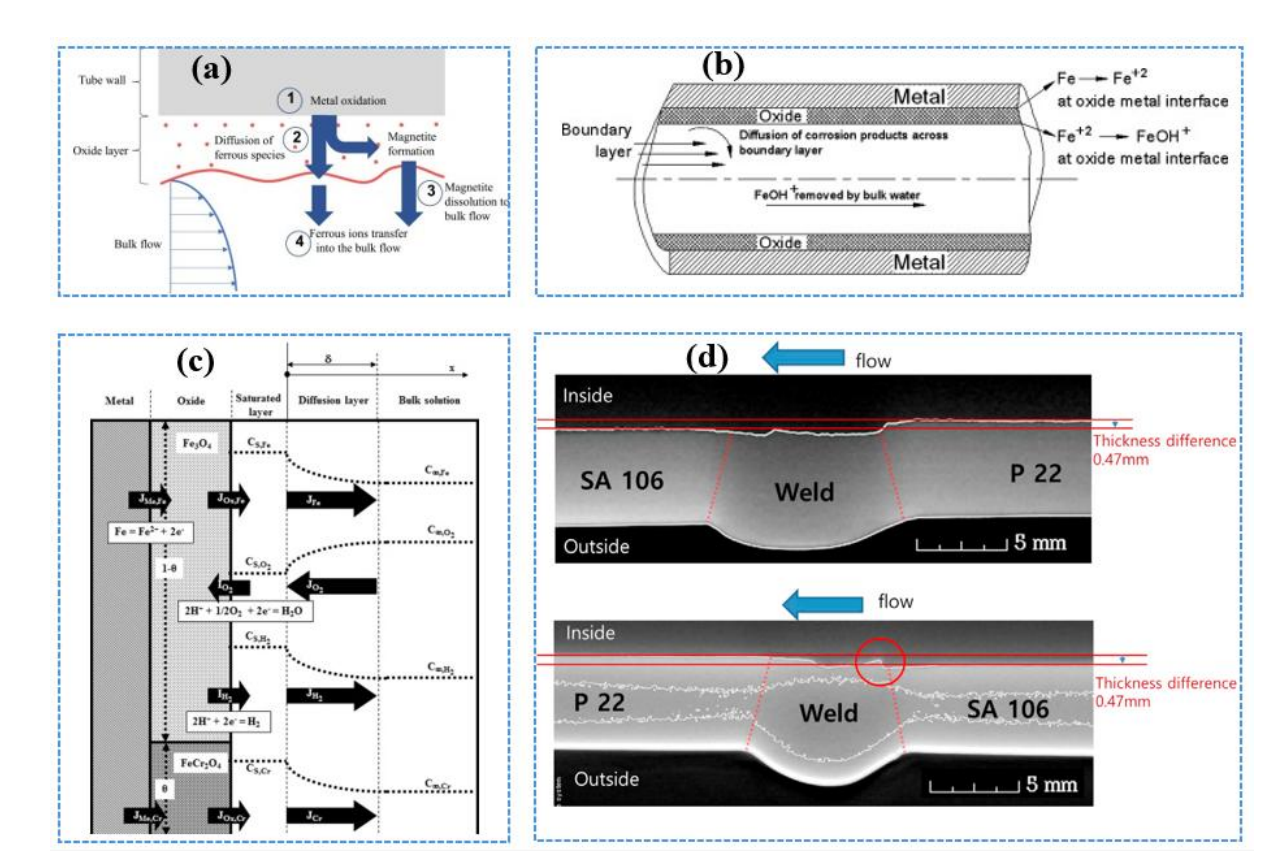


Figure 2: Illustrations and images of FAC Mechanisms: (a) Four key stages of the dissolution process include oxidation of metal, ferrous species diffusion, magnetite formation, and transport of ions to the bulk flow and pipe; (b) Schematic of diffusion across the boundary layer (Fe²⁺, FeOH⁺ removal). (c) The physicochemical model of the oxide layer for FAC during the dissolution process. (d) Computed tomography of P22 and SA105 of the welded joint with the flow in the P22-SA106 and SA106-P22 (marked in the figure) after 7200 h. (Reprinted from references [35], [5], [16], and [24] with copyright permission).

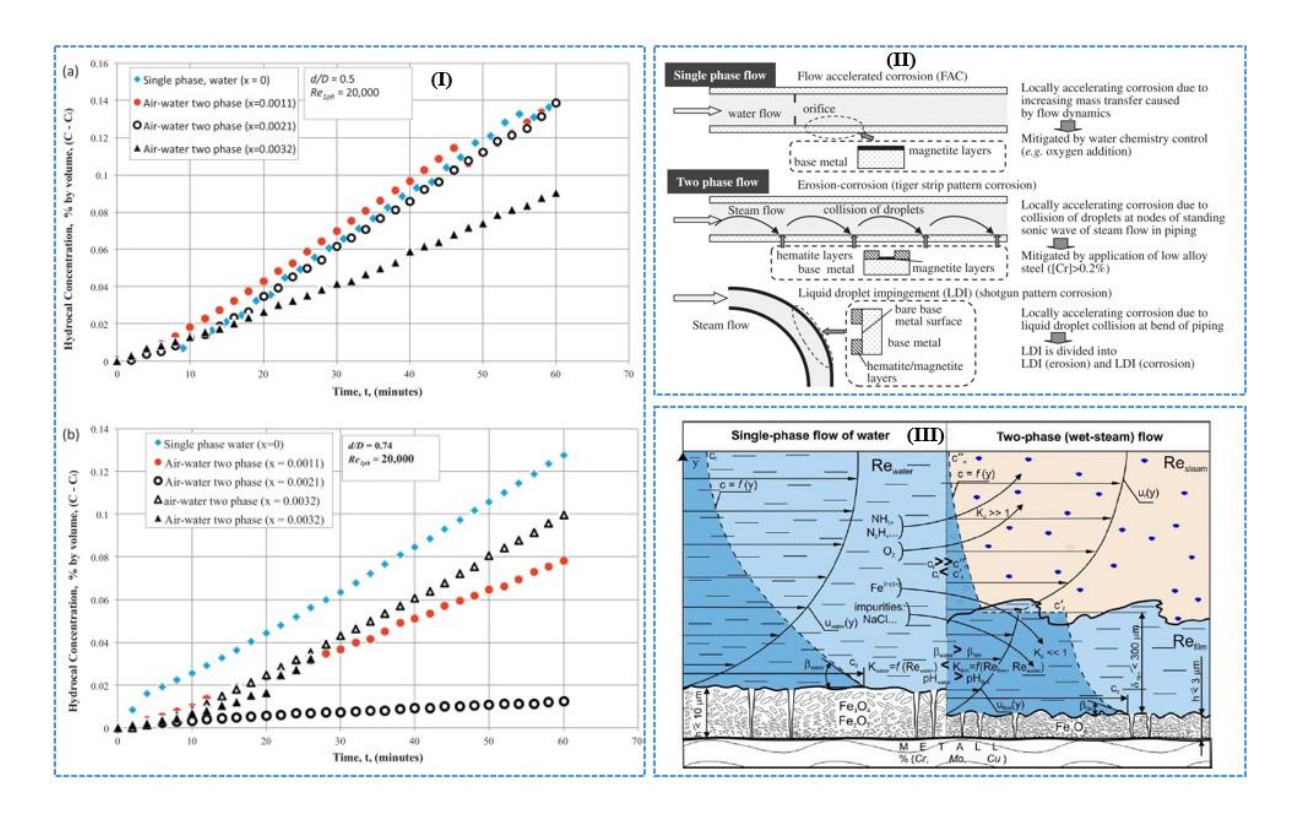


Figure 3: Key characteristics and mechanisms of wall thinning under single- and two-phase flow conditions. (I) time-dependent ferrous species release (Hydraulic concentration curves) under single- and two-phase flow for different orifice-to-pipe diameter ratios (a) 0.5, (b) 0.74. (II) Schematic of wall thinning morphologies-single-phase chevron/tiger-striping vs. two-phase droplet impingement. (III) Comparative mechanisms of FAC driven by single-phase and two-phase hydrodynamics. (Reprinted from references [17], [44] and with copyright permission).

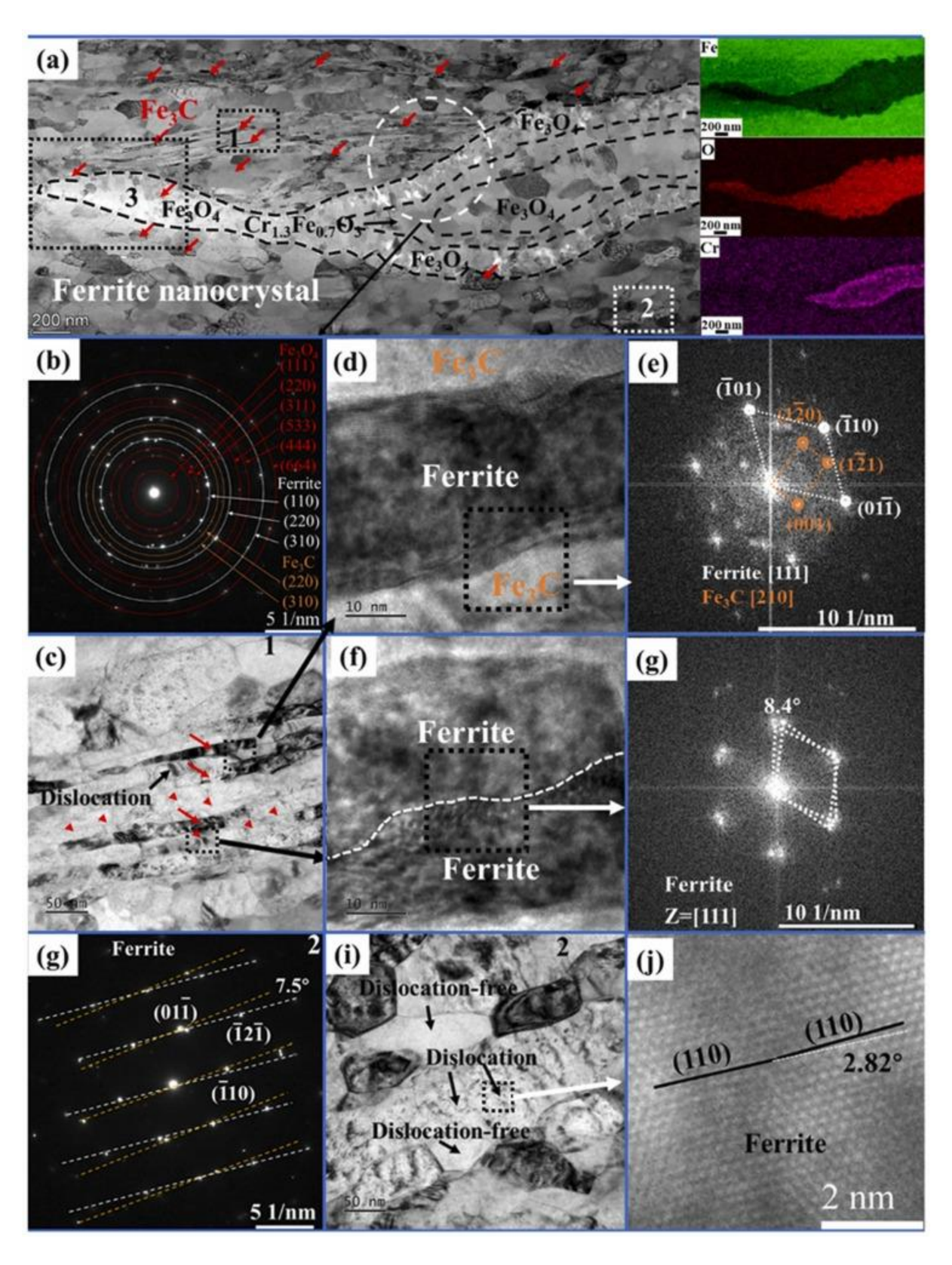


Figure 4: (a) High-magnification BE-TEM image with EDX elemental maps of Fe, O, and Cr for samples machined from a SA106B pipe used in PWR; (b) Corresponding SAED pattern from the selected region in (a); (c) Magnified BE-TEM view of region 1 in (a); (d) HR-TEM image from the boxed area in (c); (e) FFT pattern derived from the region in (d); (f) Additional HR-TEM image from a boxed zone in (c); (g) FFT pattern from the selected region in (f); (h)

SAED pattern from area 2 in (a); (i) Enlarged BE-TEM image of region 2 in (a); (j) HR-TEM image showing fine structural details from (i) . (Reprinted from references [39] with copyright permission).

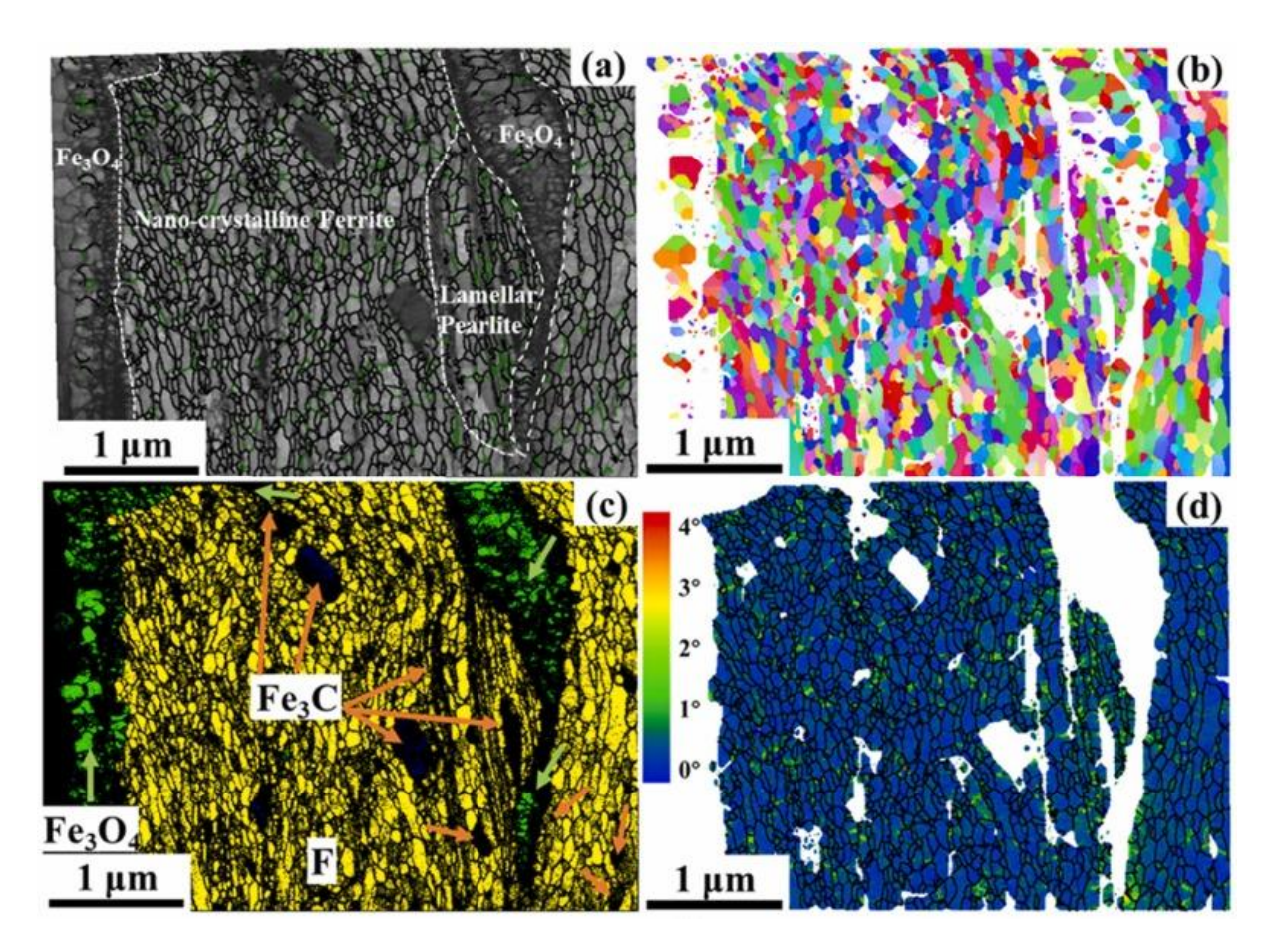


Figure 5: (a) Band contrast (BC) image overlaid with grain boundaries, highlighting nanocrystalline ferrite and lamellar pearlite; (b) Inverse pole figure (IPF) map showing crystallographic orientation of grains; (c) Phase map distinguishing ferrite and cementite (Fe₃C), with Fe₃O₄ regions labeled; (d) Kernel average misorientation (KAM) map indicating local strain gradients. (Reprinted from reference [39] with copyright permission).

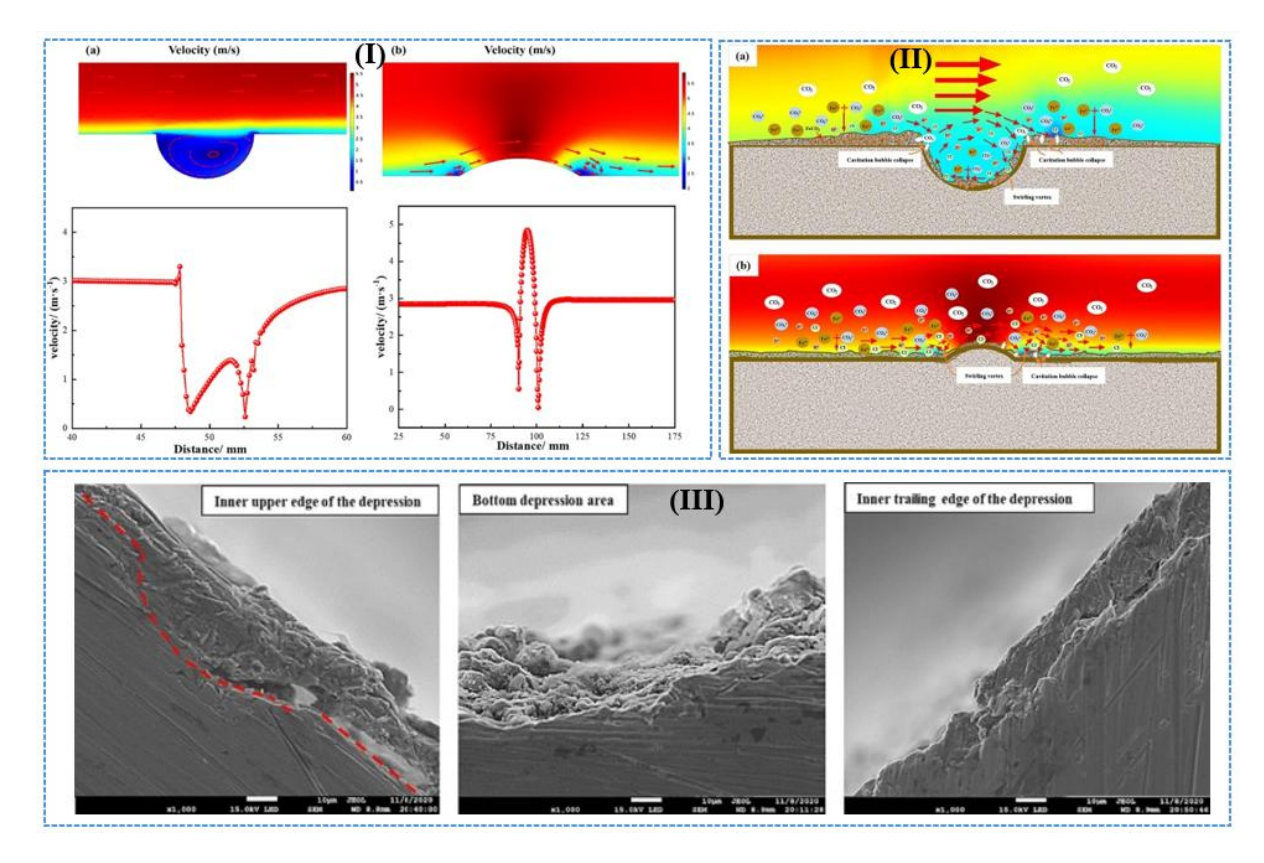


Figure 6: Influence of local flow disturbances and micro-turbulence on mass transfer and corrosion mechanisms: (I) Flow field distribution near surface defects. (II) Schematic representation of mass transfer and corrosion interactions under micro-turbulent conditions. (III) Cross-sectional microstructural damage observed in flow-depressed regions. (Reprinted from reference [45] with copyright permission).

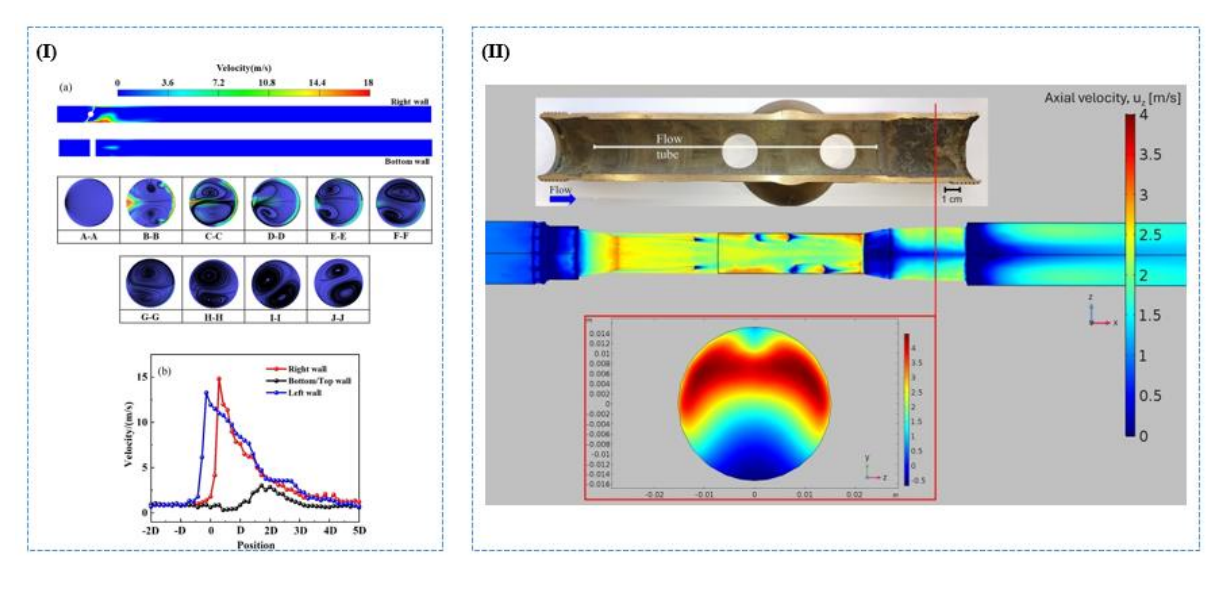


Figure 7: CFD simulation of velocity profiles and flow distribution in complex geometries relevant to FAC conditions: (I) Velocity distribution and wall-based comparisons in a simulated pipe system, and (II) Axial velocity field and cross-sectional view in a dual-orifice flow tube. (Reprinted from references [98] and [100] with copyright permission).

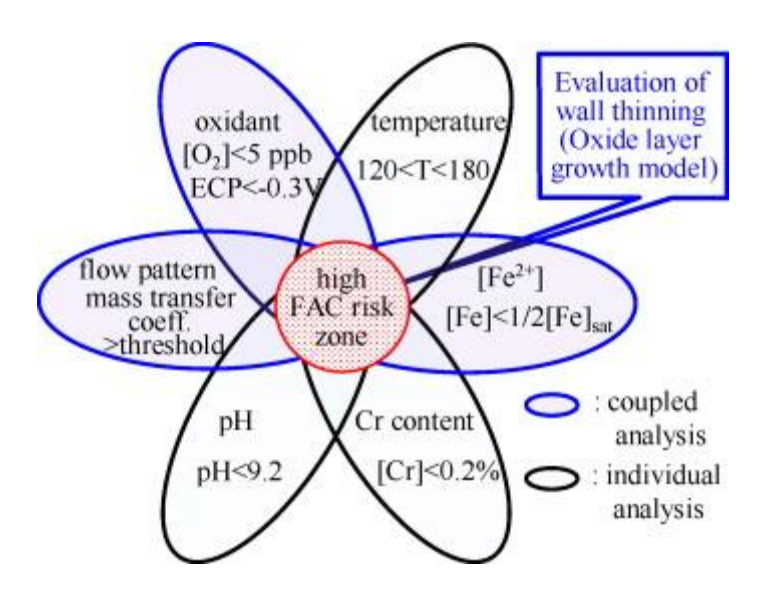


Figure 8: Key parameters governing the high-risk zone for FAC. (Reprinted from reference [46] with copyright permission).

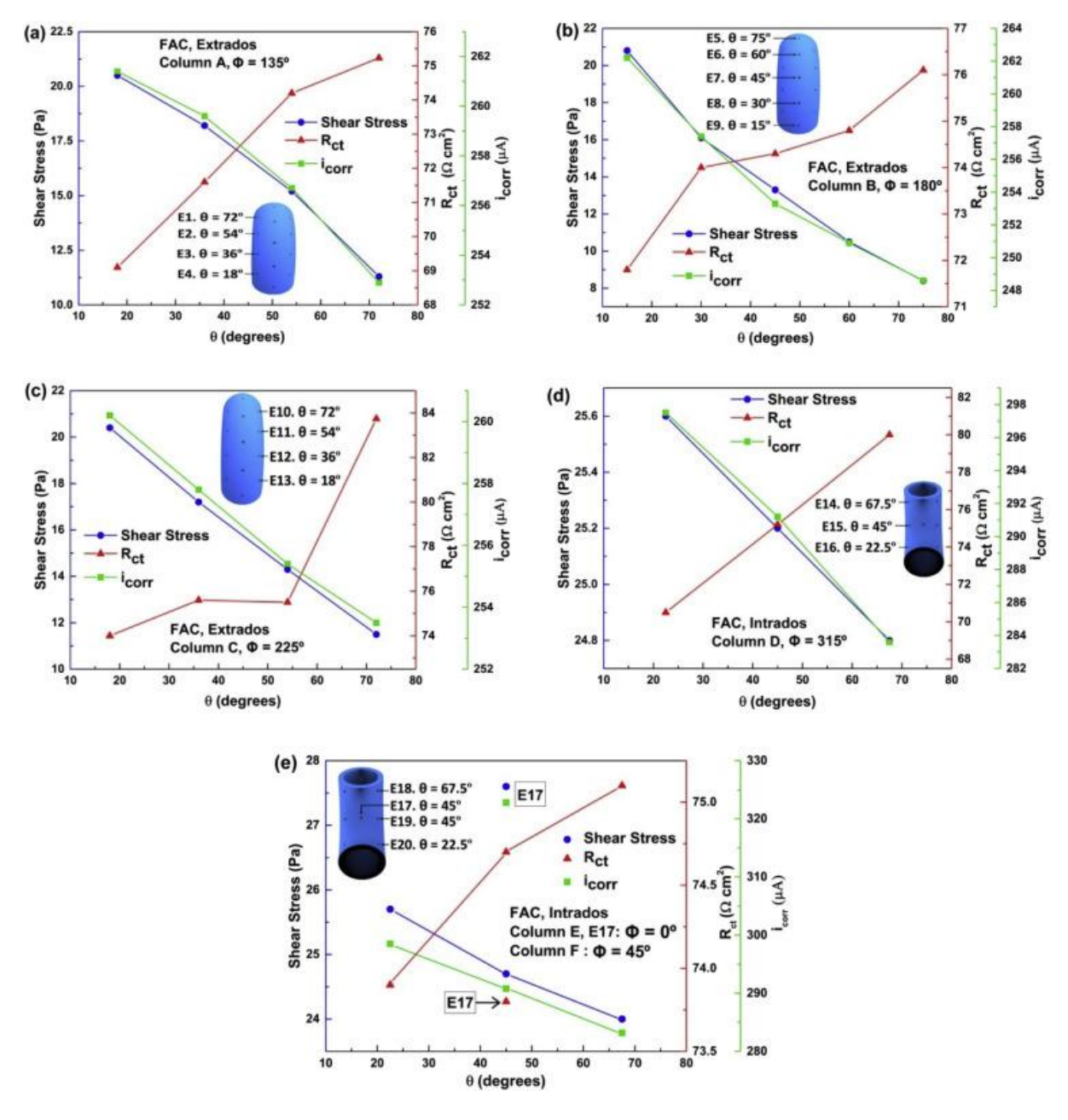


Figure 9: Variations in shear stress, $R_{\rm ct}$, and $i_{\rm corr}$ along the flow path on working electrodes positioned at different azimuthal angles (φ) of the elbow during FAC testing: (a) $\varphi = 135^{\circ}$, (b) $\varphi = 180^{\circ}$, (c) $\varphi = 225^{\circ}$, (d) $\varphi = 315^{\circ}$, and (e) $\varphi = 0^{\circ}$ and 45°. (Reprinted from reference [38] with copyright permission).

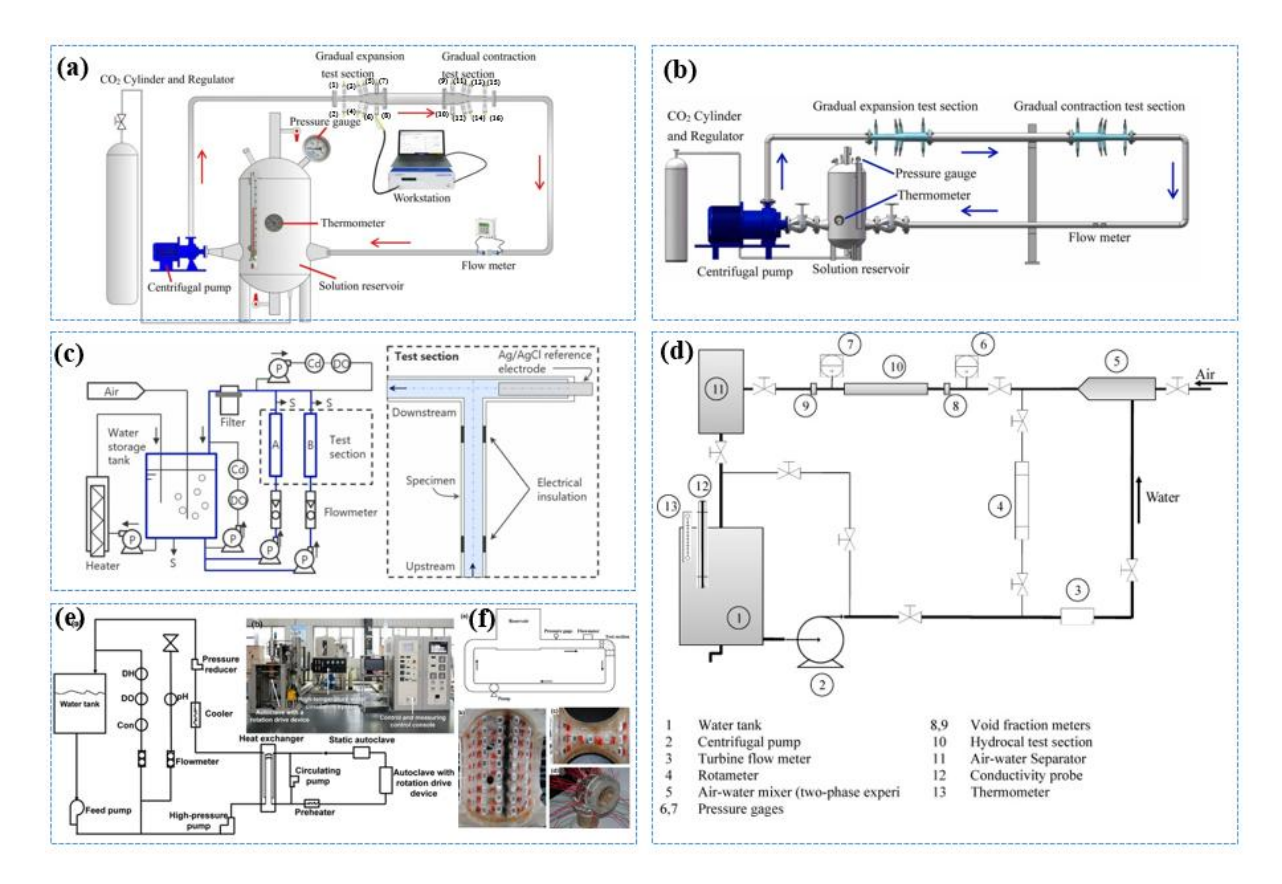


Figure 10: Various experimental flow loop setups used for simulating FAC conditions. (a) HPFL apparatus with (a) and without an electrochemical work-station. (c) HPFL setup with conductivity and DO sensors. (d) HPFL setup with an air-water mixer. (e) HPFL setup with static autoclave [188]. (f) HPFL setup with an array electrode configuration. (Reprinted from references [191], [47], [43], [58] and [63] with copyright permission).

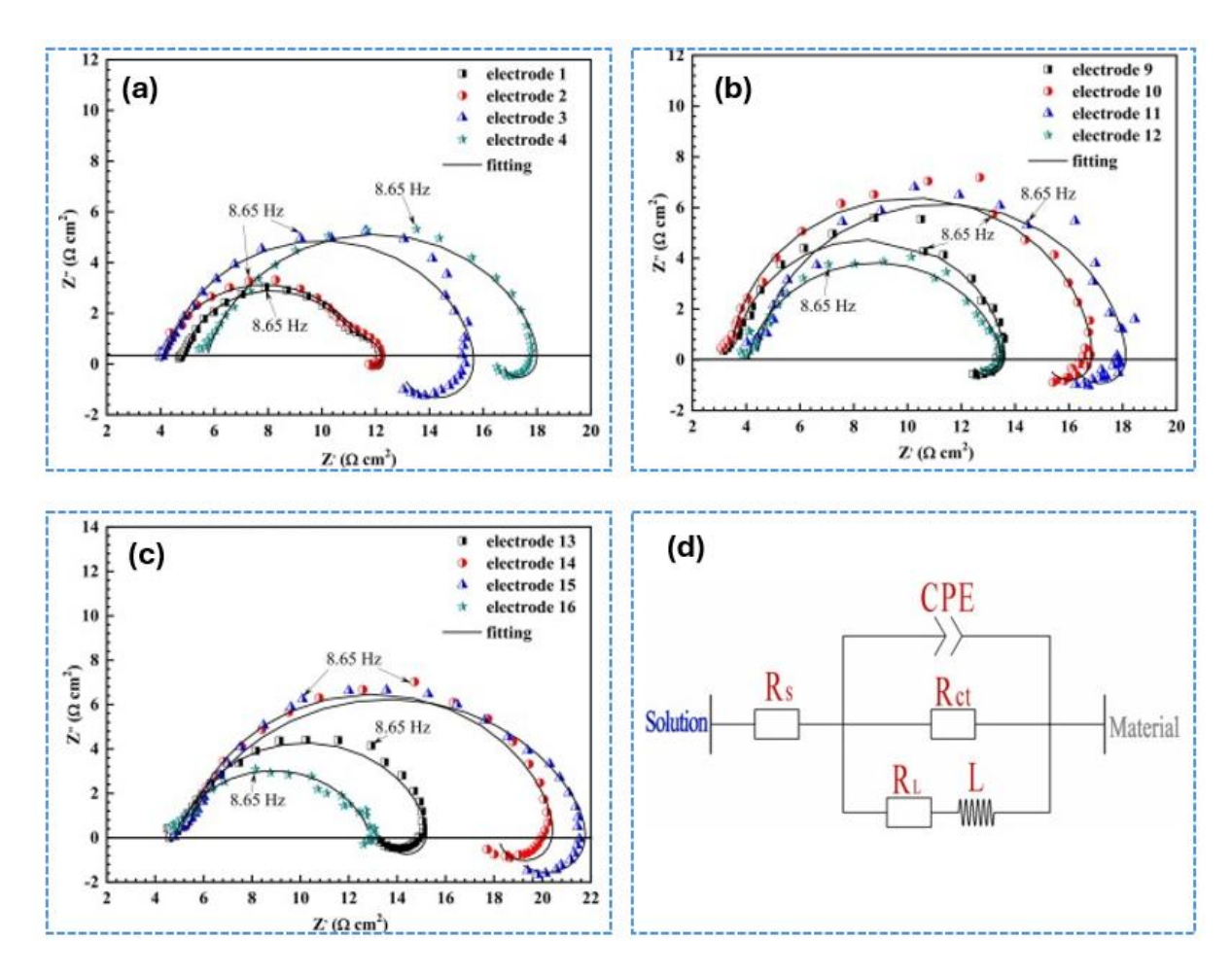


Figure 11: Nyquist plot for X65 carbon steel electrodes located at different positions within the flow loop: (a) Top of the gradual contraction pipe, (b) Top of the gradual expansion pipe, and (c) Bottom of the gradual expansion pipe. (d) The corresponding electrochemical equivalent circuit used for fitting the EIS data. (Reprinted from reference [23] with copyright permission).

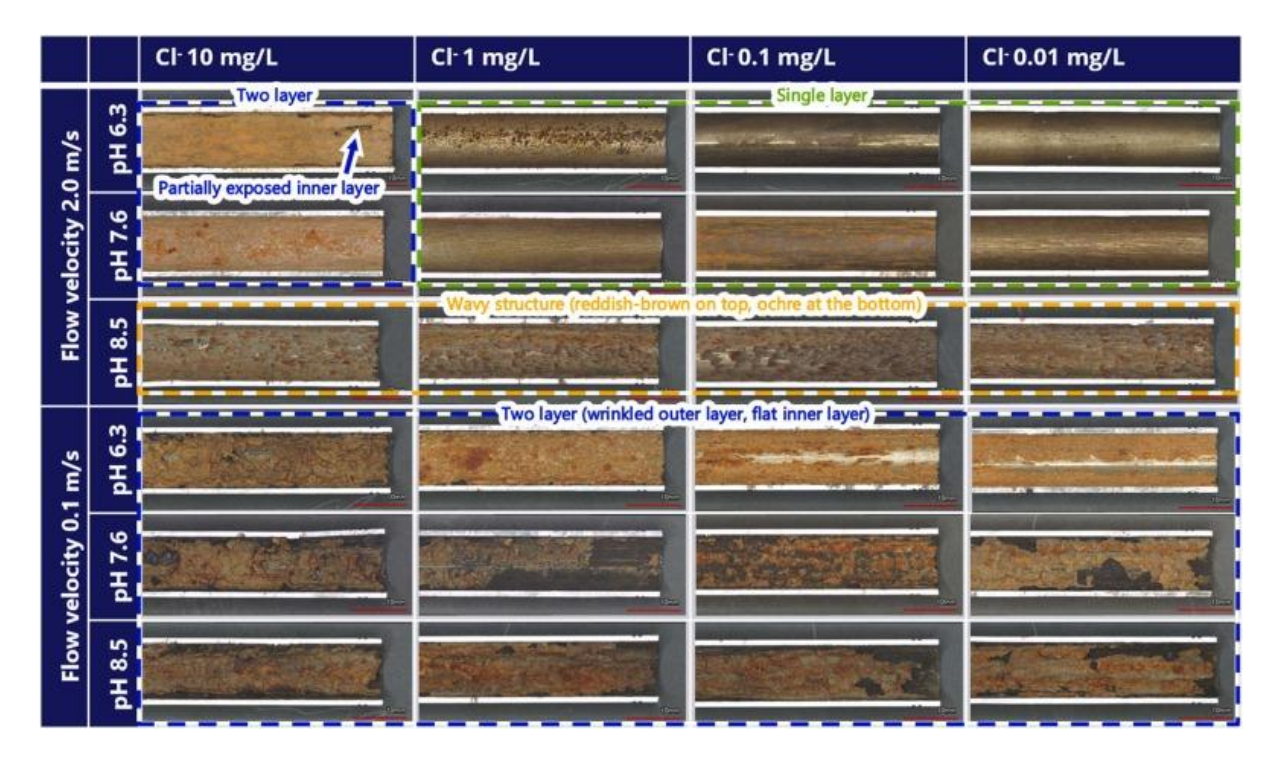


Figure 12: Visual comparison of surface degradation of carbon steel exposed to various chloride ion concentrations (Cl⁻: 10, 1, 0.1, and 0.01 mg/L), pH levels (6.3, 7.6, 8.5), and flow velocities (0.1 and 2.0 m/s). (Reprinted from reference [43] with copyright permission).

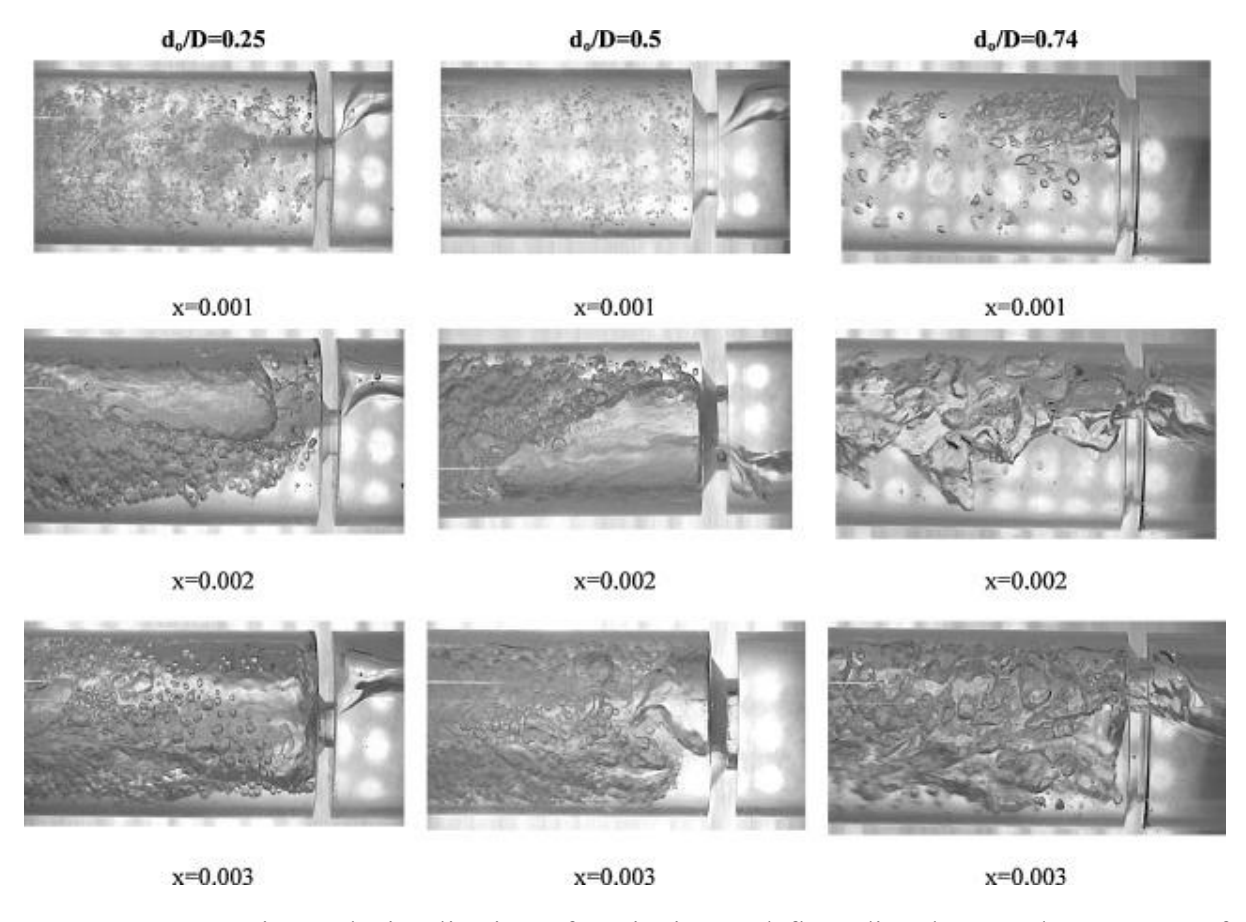


Figure 13: Experimental visualization of cavitation and flow disturbances downstream of orifices with different diameter ratios ($d_o/D = 0.25$, 0.5, and 0.74) and axial locations (x = 0.001 to 0.003). (Reprinted from reference [17] with copyright permission).

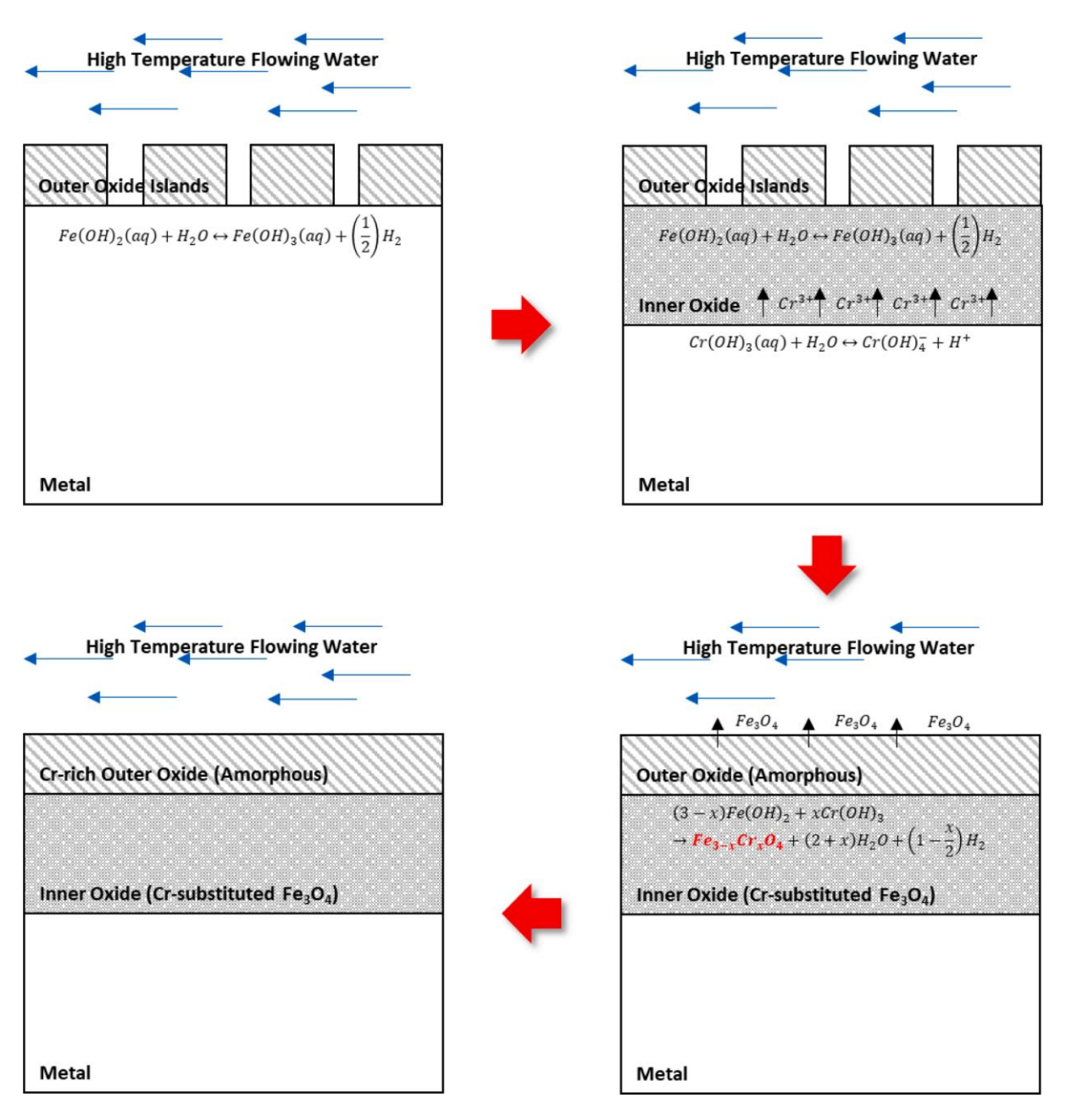


Figure 14: Formation mechanism of Cr-enriched bi-layer oxide films on low-alloy steels improving the anti-FAC resistance against high-temperature flowing water, (Reprinted from reference [23] with copyright permission).

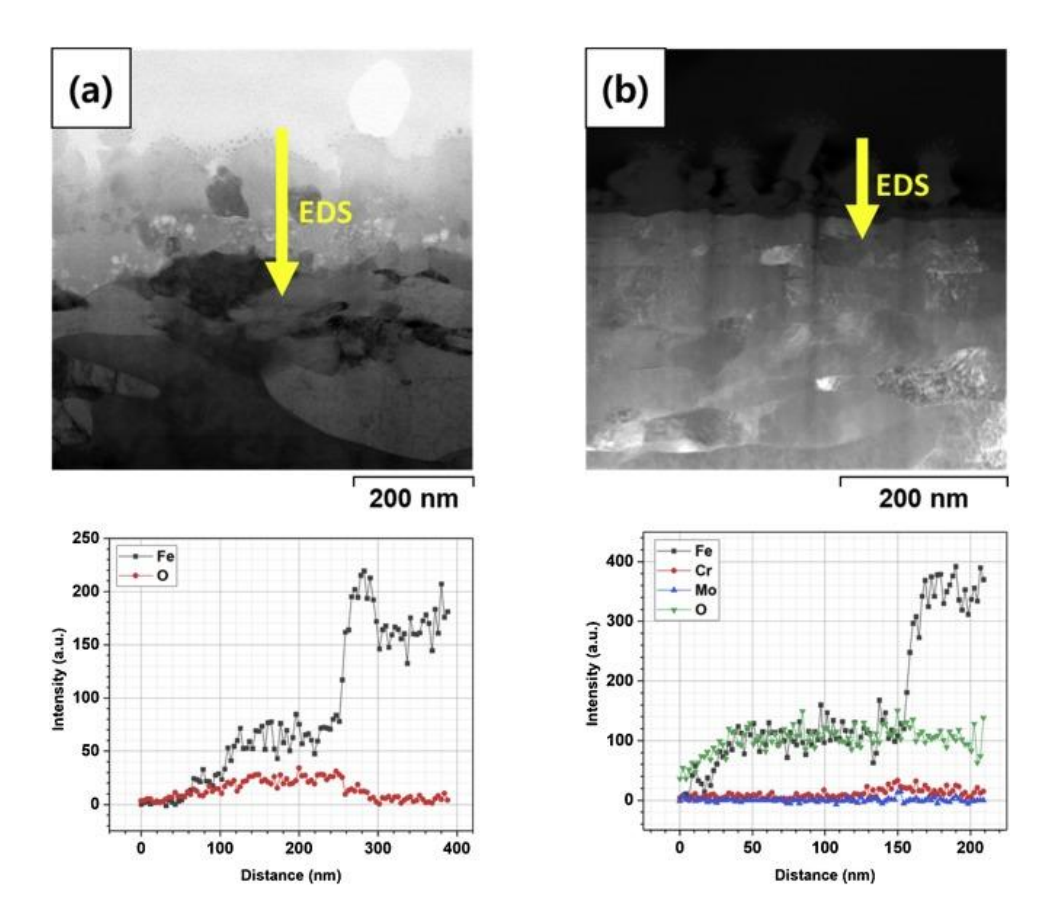


Figure 15: TEM and EDS profiles of SA516 (a) and P22 (b) showing the effect of Cr and Mo on the oxide layer structure of low-alloy steels. (Reprinted from reference [71] with copyright permission).

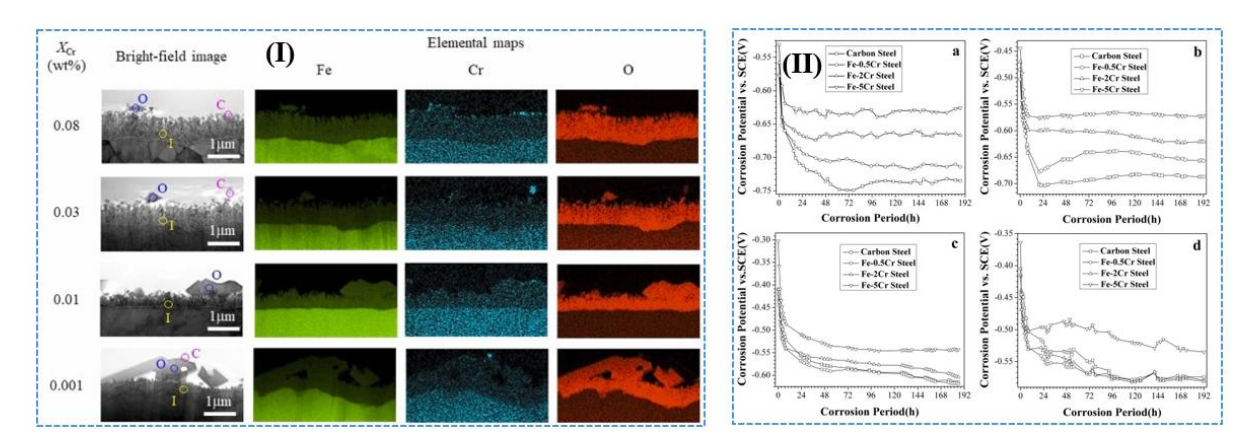


Figure 16: (I) SEM images and elemental maps (Fe, Cr, O) showing the oxide layer structure on steels with varying Cr content (xCr: x=0.001~0.08) after exposure to 3.5% NaCl. (II) Variation of corrosion potential for carbon steels with different Cr content (xCr: x=0~5) under different flow conditions: (a) stagnant, (b) 0.4 m/s, (c) 0.8 m/s, and (d) 1.6 m/s. (Reprinted from references [30] and [74] with copyright permission).

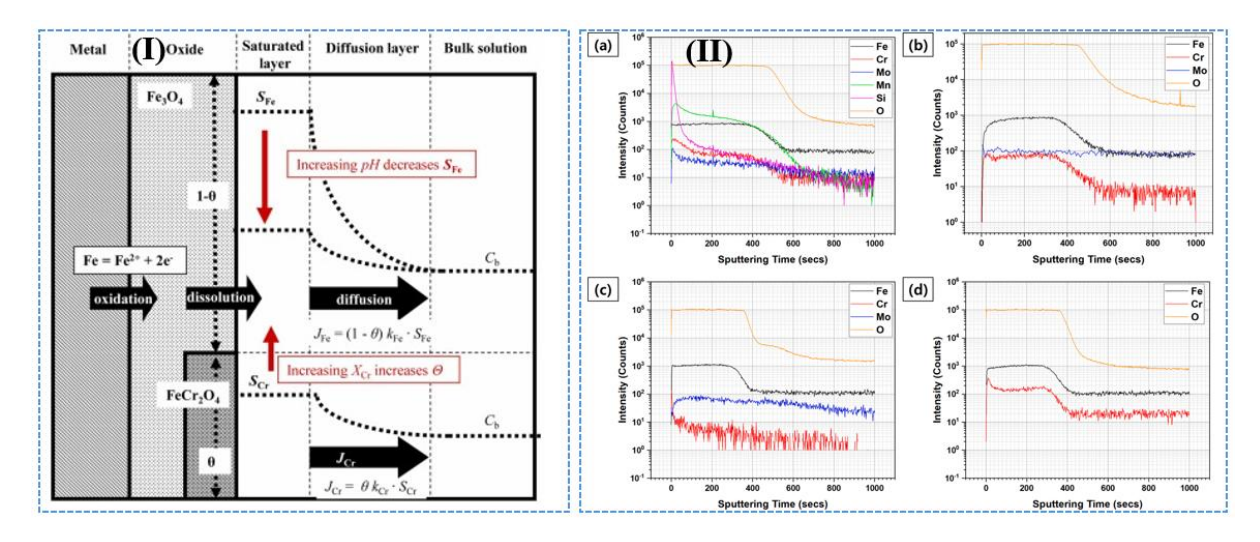


Figure 17: Effect of pH and Cr content on FAC resistance of carbon steels. (I) Schematic model showing the impact of pH and Cr content (*x*Cr) on solubility and diffusion of Fe. (II) ToF-SIMS depth profiles of oxide films formed on different alloys after FAC test: (a) P22, (b) FRA 1, (c) FRA 2, (d) MFRA. (Reprinted from references [30] and [23] with copyright permission).

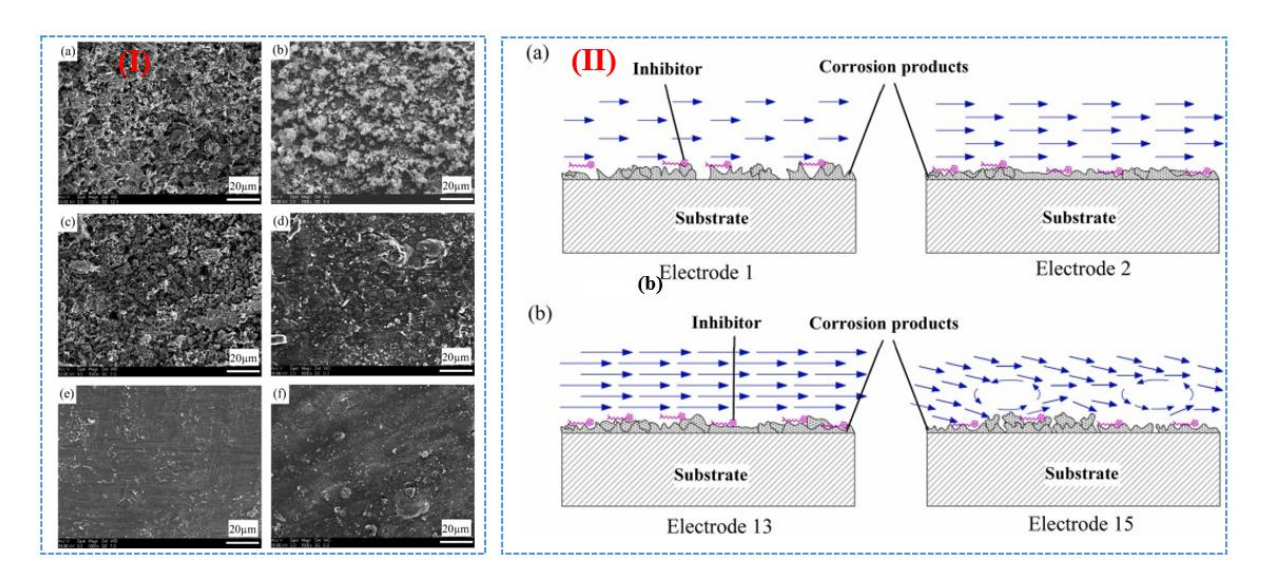


Figure 18: Chemical inhibitors: (I) SEM images of X65 carbon steel with different thioureidoimidazoline concentrations (a) 0, (b) 1 mg/L, (c) 10 mg/L, (d) 50 mg/L, (e) 100 mg/L, and (f) 200 mg/L. (II) FAC mechanism in contraction (a), expansion zones (b). (Reprinted from references [27] and [47] with copyright permission).



Figure 19: Future research perspectives and directions for flow-accelerated corrosion (FAC).